

A Sponsored Supplement to *Science*

Smarter imaging: Gaining more from your microscopy experiments



Sponsored by

Produced by the
Science/AAAS Custom
Publishing Office



Science
AAAS

ScienceAdvances

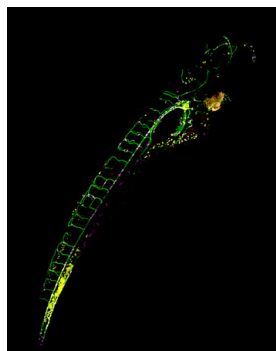


OPEN ACCESS, DIGITAL, AND FREE TO ALL READERS



Pushing the Boundaries of Knowledge

As AAAS's first multidisciplinary, open access journal, *Science Advances* publishes research that reflects the selectivity of high impact, innovative research you expect from the *Science* family of journals, published in an open access format to serve a vast and growing global audience. Check out the latest findings or learn how to submit your research: [ScienceAdvances.org](https://www.scienceadvances.org)



About the cover: Larval zebrafish (fli1a:dsRed x myl7:gfp) image captured in a single FOV with a Nikon Plan Apo Lambda 4x objective and A1R HD25 confocal. Sample courtesy of Martha Marvin, Ph.D., Williams College.

This booklet was produced by the *Science*/AAAS Custom Publishing Office and sponsored by Nikon Instruments Inc.

Editors: Jackie Oberst, Ph.D.; Sean Sanders Ph.D.
Proofreader/Copyeditor: Bob French
Designer: Amy Hardcastle

LAURIE FARADAY,
ASSOCIATE SALES DIRECTOR-US
Custom Publishing
Science/AAAS
lfaraday@aaas.org
Tel: 508-747-9395

© 2018 by The American Association
for the Advancement of Science.
All rights reserved. 7 December 2018

Smarter imaging: Gaining more from your microscopy experiments

INTRODUCTIONS

2 Seeing the bigger picture: High-throughput live-cell imaging

Jackie Oberst, Ph.D.
Sean Sanders, Ph.D.
Science/AAAS

3 Designing better imaging experiments for more meaningful data

Lynne Chang, Ph.D.
Nikon Instruments Inc.

WHITE PAPER

4 Increasing data collection and fidelity by maximizing confocal field of view

Adam White, Ph.D.
Biosystems Product Manager,
Confocal and Super-Resolution
Nikon Instruments Inc.

RESEARCH ARTICLES

6 Analysis of the bystander effect in cone photoreceptors via a guided neural network platform

Yuan Ma, Xin Han, Ricardo Bessa de Castro *et al.*

14 Bacteria as living patchy colloids: Phenotypic heterogeneity in surface adhesion

Teun Vissers, Aidan T. Brown, Nick Koumakis *et al.*

22 Programming self-organizing multicellular structures with synthetic cell-cell signaling

Satoshi Toda, Lucas R. Blauch, Sindy K. Y. Tang *et al.*



Seeing the bigger picture: High-throughput live-cell imaging

Several microscopy methods have arisen that enable researchers to study living cells in more detail and with less effort than ever before.

Imagine a tissue culture dish with cells growing on it as an Olympic-sized swimming pool with inner tubes strewn across it. Previously, investigators analyzing those cultures were only able to choose a handful of these metaphorical inner tubes in a few particular areas, such as one or two “swimming lanes,” and had to leave the rest. Now, with the advent of higher-throughput imaging techniques, they can measure the entire swimming pool.

Several microscopy methods have arisen that enable researchers to study living cells in more detail and with less effort than ever before. Live single-cell imaging is the study of individual living cells using time-lapse microscopy. Live imaging, of both individual cells and groups of cells and tissues, has become an essential tool in most cell biology laboratories, and is used in numerous biomedical fields, such as neurobiology, developmental biology, and pharmacology.

One of the major advancements in live-cell imaging has been in increasing throughput. By integrating robotic microscopy and automated analysis methods with live-cell imaging, researchers are now able to gather more accurate statistics and population-level data at single-cell level resolution.

Recent developments in imaging technologies such as confocal and superresolution are now allowing researchers to enhance their live-cell high-throughput experiments by applying these techniques. For example, capturing images of large samples—such as tissues, live model organisms, or single cells in multiwell plates—requires extending the detection area or field of view (FOV) and increasing the image capture speed. An increased FOV reduces the image acquisition time as well as the number of frames needed for stitching large images and achieving high-throughput imaging of large-scale samples.

The articles in this supplement reflect the latest single-cell and live-cell imaging techniques. We hope they encourage those who haven’t already done so to dip their toes into the water and try these methods, or inspire those who already use these techniques to venture further and deeper.

Jackie Oberst, Ph.D.

Sean Sanders, Ph.D.

Custom Publishing Office
Science/AAAS



Designing better imaging experiments for more meaningful data

Imaging experiments have been trending toward higher-content approaches in order to delve deeper into the mechanism and increase data fidelity.

“**W**hat is the mechanism?” This is a fundamental question that drives many biological research programs. Imaging experiments have been trending toward higher-content approaches in order to delve deeper into the mechanism and increase data fidelity. In this digital supplement, we highlight several recent studies from researchers who not only use high-throughput methods but combine them with novel engineering techniques, whether at the specimen or platform level, to gain more from their imaging experiments.

In the first study, Ma *et al.* describe an ordered neural network guided by microchannels (NN-Chip) to study the bystander effect at the single-cell level. Using this NN-Chip, the authors could directly visualize apoptosis spreading from light-induced apoptotic cone cells to the surrounding cones. This micropatterned platform enables high-efficiency patterning of neural networks and alleviates challenges for dissecting the mechanism of the bystander effect, holding great potential for other neuronal studies. Highly ordered specimens that result from these types of micropatterned substrates would also lessen challenges in image processing and analysis. In the second study, Vissers *et al.* follow many single cells using high-throughput tracking and big data analysis to study bacterial adhesion properties. This approach is unlike many biophysical studies of bacterial adhesion that use either high-throughput, population-level methods or low-throughput, single-cell studies. In the third study, Toda *et al.* engineer artificial genetic programs to study the role of cell-cell signaling in the formation of self-organizing multicellular structures. The authors show that minimal intercellular programs are sufficient to yield complex assemblies of cells that mimic natural developmental systems.

The studies we have highlighted stand apart from standard high-throughput experiments in which single cell-level detail is generally sacrificed for population-level data. To meet the demands of single-cell level, high-throughput experiments, Nikon has developed a new point-scanning confocal microscope with the largest field of view (FOV) on the market. With its 25-mm FOV, Nikon’s A1R HD25 captures almost twice the data of conventional confocal systems in a single frame. This new capability not only increases the speed and throughput of imaging experiments, but enables researchers to carry out high-throughput experiments using high-resolution, high-magnification lenses to capture more detail without sacrificing speed. In this supplement we have included a white paper detailing the application benefits of the A1R HD25.

We hope the content provided here provides insights into how high-throughput imaging methods are being used in various scientific fields, and inspires readers to think about ways to gain more data from their imaging experiments.

Lynne Chang, Ph.D.
Senior Marketing Manager
Nikon Instruments Inc.

Increasing Data Collection and Fidelity by Maximizing Confocal Field of View

Summary

For years, the field of view (FOV) of confocal systems have been limited by the FOV of the microscope they are attached to. With the release of the Nikon Ti2 inverted microscope, the world's first 25 mm FOV became available. Now, Nikon has taken advantage of this improvement by building the largest FOV point scanner in the world, the A1R HD25. This application note will focus on the impact of this technology on simple, everyday experiments.

Introduction

Microscope-based image creation is an important research tool that has continually evolved since the 1600s. Today's systems utilize a variety of technologies, such as high-end cameras, LEDs, lasers, and confocal point scanners, with the goal of acquiring better data. As part of this, there has been a recent push to increase throughput of these systems so that more data can be produced with less time in front of the system. For confocal fluorescence microscopy, much of this innovation has centered on making systems faster and more sensitive. However, since fluorescent samples have a limited photon budget, these approaches reach a practical limit as too much laser power is applied and/or not enough signal is generated.

Recognizing these limits, Nikon has worked to go beyond our market-leading speed, sensitivity, and image quality in targeting an additional approach to throughput: making a bigger picture. Utilizing the astounding optical quality of Nikon glass, new, larger optical components have been created to increase the standard confocal microscope system FOV to an incredible 25 mm. This application note focuses on the impact of this increased FOV on everyday research and will show why the Nikon A1R HD25 is the new standard in confocal microscopy.

Increased field of view significantly increases cell counts in a single image

One of the most common types of microscope imaging experiments is a simple cell-count assay. These assays are performed in a variety of ways, and used to investigate questions pertaining to cell or tissue growth/death, the impacts of drug treatments, and

the impacts of environmental/applied stresses. When the desired model for such an experiment is best suited for analysis with a microscope, a researcher must create samples for all conditions and proceed to collect images from each. Image analysis is then required to count cells for each condition. In most cases, this type of experiment means sitting in front of the microscope and capturing enough images for each condition to produce a high-enough cell count (n) to address a given question. So, how does FOV impact this common microscope system use case?

Figure 1 shows a representative comparison of data produced when using both a 25 mm FOV and a 18 mm FOV to count nuclei in a single field. For the 18 mm FOV (shown in Panel **A**), 76 cells are counted in this frame. By simply increasing the FOV to 25 mm and capturing the same image, this count jumps to 149 cells (shown in Panel **B**). Immediately, one can see that this small improvement in FOV can lead to collection of nearly *twice* the data in every single image. Such an impact has the potential to cut experiment time in half by requiring the collection of fewer images in order to achieve the same n . Say, for this example, that an n of 1,500 cells is desired for each condition. With the 25 mm FOV, this can be achieved with ~10 images while, at 18 mm, about 20 images are needed for *every condition* to achieve the same counts.

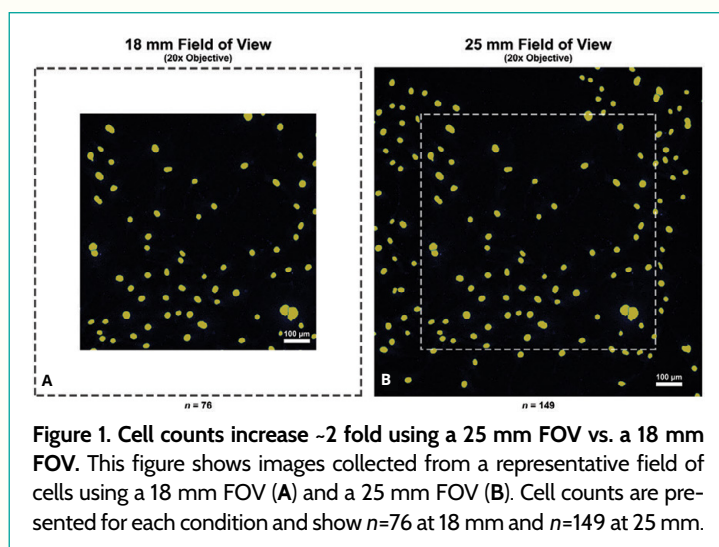


Figure 1. Cell counts increase ~2 fold using a 25 mm FOV vs. a 18 mm FOV. This figure shows images collected from a representative field of cells using a 18 mm FOV (A) and a 25 mm FOV (B). Cell counts are presented for each condition and show $n=76$ at 18 mm and $n=149$ at 25 mm.

Adam White, Ph.D.

Biosystems Product Manager, Confocal and Super-Resolution
Nikon Instruments Inc., 1300 Walt Whitman Road, Melville, NY 11747-3064, USA

Increased field of view provides higher cell counts, better statistics over whole experiments

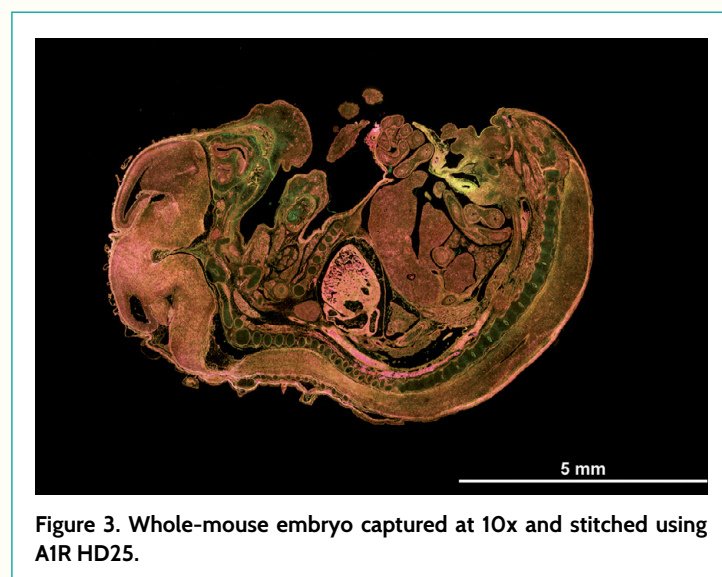
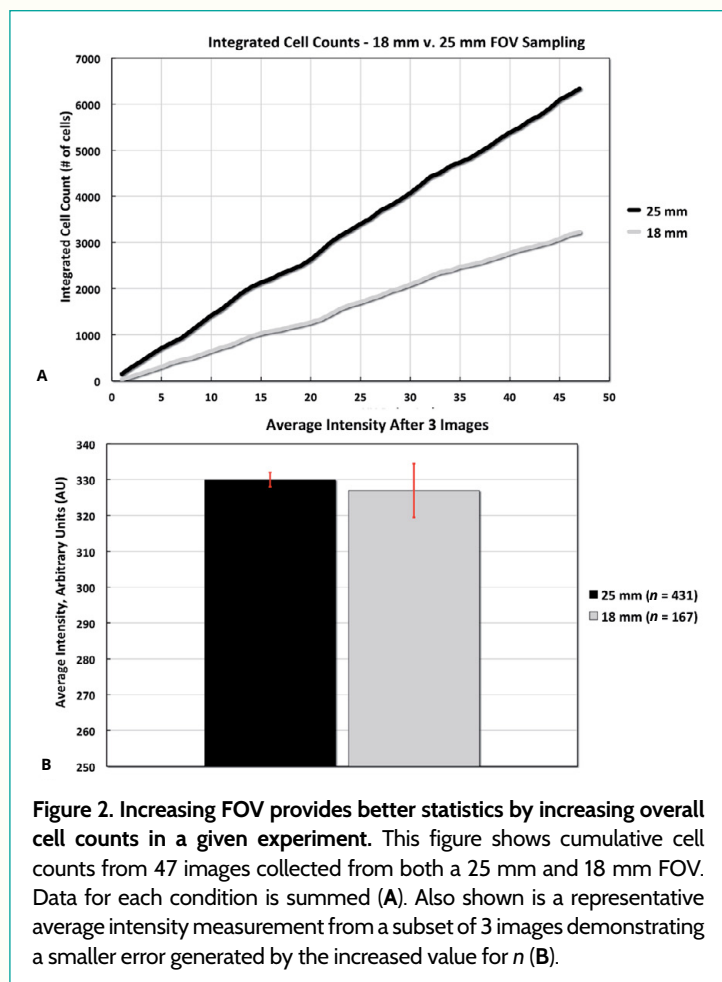
Of course, saving time may not always be the goal when generating data for a confocal microscopy experiment. Take, for example, a study in which a subtle change has occurred under a particular condition but, when statistical analysis is applied, the results are inconclusive. In this situation, increasing population size, n , may help generate enough confidence to draw a conclusion. **Figure 2** shows the cumulative effect of increased FOV on cell count during an experiment in which 47 images were collected at both 18 mm and 25 mm. First, the obvious conclusion based on the data presented above is that the cumulative cell count over these 47 images increases much more rapidly with the 25 mm FOV (Panel A). In this case, average intensity measurements were collected from a subset of these images as well (Panel B). The less obvious conclusion, though just as important, is that collecting more data simply by virtue of having a larger FOV means that, in the same number of images, the much larger n produced leads to less statistical error (represented as error bars in Panel B). In other words, capturing

data with a large FOV drives a more rapid decrease in relative uncertainty as the total image count increases. Lower uncertainty means that better conclusions can be drawn when the experimental results are collated. A1R HD25 is about using the available tools and technology to produce better data, and more of it, resulting in more impactful research.

Conclusion

Importantly, while not covered in this note, the Nikon A1R HD25 can benefit many applications beyond cell counting. For example, the same improvements described above can be applied to confocal high-content screening. This will result in the highest throughput system of its kind, by maximizing data collection in every image. In the case of large model organisms such as zebrafish embryos, one may be able to image the whole organism in a single FOV, and at a higher magnification than was previously achievable. Getting the whole picture allows the user to capture details at higher magnification and resolution than previously possible with a given size FOV. Large image stitching is another common application for confocal microscopes. With A1R HD25, the large FOV not only allows for the generation of stitched images more quickly, but the complete optical redesign means that these images are created with fewer artifacts (example shown in **Figure 3**).

With the world's first 25 mm FOV, the Nikon A1R HD25 is the latest in point-scanning confocal technology. The data and examples described above have shown how this simple, yet important optical change can allow researchers to optimize time spent in front of the microscope. The A1R HD25 means more and better data in every image, every day.



CELLULAR NEUROSCIENCE

Analysis of the bystander effect in cone photoreceptors via a guided neural network platform

Yuan Ma,^{1,2,3} Xin Han,^{1,3} Ricardo Bessa de Castro,^{1,3,4} Pengchao Zhang,^{1,3} Kai Zhang,^{1,3} Zhongbo Hu,² Lidong Qin^{1,3*}

The mammalian retina system consists of a complicated photoreceptor structure, which exhibits extensive random synaptic connections. To study retinal development and degeneration, various experimental models have been used previously, but these models are often uncontrollable, are difficult to manipulate, and do not provide sufficient similarity or precision. Therefore, the mechanisms in many retinal diseases remain unclear because of the limited capability in observing the progression and molecular driving forces. For example, photoreceptor degeneration can spread to surrounding healthy photoreceptors via a phenomenon known as the bystander effect; however, no in-depth observations can be made to decipher the molecular mechanisms or the pathways that contribute to the spreading. It is then necessary to build dissociated neural networks to investigate the communications with controllability of cells and their treatment. We developed a neural network chip (NN-Chip) to load single neurons into highly ordered microwells connected by microchannels for synapse formation to build the neural network. By observing the distribution of apoptosis spreading from light-induced apoptotic cones to the surrounding cones, we demonstrated convincing evidence of the existence of a cone-to-cone bystander killing effect. Combining the NN-Chip with microinjection technology, we also found that the gap junction protein connexin 36 (Cx36) is critical for apoptosis spreading and the bystander effect in cones. In addition, our unique NN-Chip platform provides a quantitative, high-throughput tool for investigating signaling mechanisms and behaviors in neurons and opens a new avenue for screening potential drug targets to cure retinal diseases.

INTRODUCTION

The structural and functional organization of the vertebrate retina is highly adapted for the initial sensing and processing of light signals, but its delicate structure also makes it vulnerable to dysfunction and diseases. The major causes of retinal diseases in adults are the progressive dysfunction and death of photoreceptors, which is induced by excessive light irradiation or mutations (Fig. 1A) (1). In most degenerative retinal diseases, such as retinitis pigmentosa and age-related macular degeneration, gap junction intercellular communication (GJIC) plays a critical role in the propagation of neuron degeneration and death via a phenomenon known as the bystander effect (2). This phenomenon—that parts of the retina degenerate and cause the deterioration of adjacent cells—severely affects neuron connections and synchronization, and gradually results in the loss of vision (3–6).

The role of the bystander effect in photoreceptor degeneration has been studied primarily *in vivo*, and the observations were made with tissue staining. Several studies have shown that mutations in the rod photoreceptors induce degeneration in adjacent cones, leading to a gradual loss of vision. The function of the photoreceptor gap junction coupling and its relation to the retina degeneration process are thus interesting to study (4, 5). Besides, maintenance of cone functions can extend most of the visual capability in patients, even in those with degenerated rod photoreceptors (7, 8). Therefore, it is important to dissect the bystander effect mechanisms between cones for potential therapeutic approaches.

In particular, the ability to study the bystander effect among photoreceptors *in vitro* has been limited by the lack of controllable models

and quantitative analysis. In tissue experimental models, the apoptosis spreading and the bystander effect cannot be discriminated from the highly coupled photoreceptor layer (9). In most cases, toxic substances may transmit through gap junctions or diffuse into cells from the surrounding matrix, which is not easy to distinguish in tissue models (4). Therefore, new models are in urgent need so that such mysteries can be deciphered in a clear, precise, and controllable mode.

Micro- and nanotechnology platforms, which use precise fabrication techniques and the physical properties of flow and operate at the micrometer scale, provide enough precision and controllability for living cell study (10, 11). These techniques should allow the production of a highly ordered neuron array and the high-throughput study of neural conduction or signal transmission between single neurons (12, 13). Here, we developed a platform using a unique microwell array interconnected by microchannels that can rapidly load single neurons in a high-throughput, user-friendly manner (Fig. 1B). Although the microwell technology has been widely used in many biological systems, it is the first time that it is perfectly implemented to neural network study and bystander killing effect exploration. To study the bystander effect at the single-cell level, we loaded single neurons into microwells to isolate neural cell bodies. Each microwell was connected to the surrounding microwells with microchannels that allowed neural communications via their synapses. To our knowledge, this platform can achieve the highest efficiency in cell loading in an up-open system and with cultured cells on a chip. Because this device created a neural network guided by microchannels, we named it neural network chip, or NN-Chip.

To investigate the bystander effect in cones, we loaded cone photoreceptor-derived 661W cells onto the NN-Chip. The 661W cells express the blue and green opsins, cone pigments, and arrestin but no rod-specific antigens, which characterize the cell line as a proper cone model for the bystander effect study (14–16). We induced apoptosis using blue light irradiation and monitored the apoptosis propagation

Copyright © 2018
The Authors, some
rights reserved;
exclusive licensee
American Association
for the Advancement
of Science. No claim to
original U.S. Government
Works. Distributed
under a Creative
Commons Attribution
NonCommercial
License 4.0 (CC BY-NC).

¹Department of Nanomedicine, Houston Methodist Research Institute, Houston, TX 77030, USA. ²College of Materials Sciences and Optoelectronics, University of Chinese Academy of Sciences, Beijing 100049, China. ³Department of Cell and Developmental Biology, Weill Cornell Medical College, New York, NY 10065, USA. ⁴College of Engineering, Swansea University, Singleton Park, Swansea SA2 8PP, UK.

*Corresponding author. Email: lqin@houstonmethodist.org

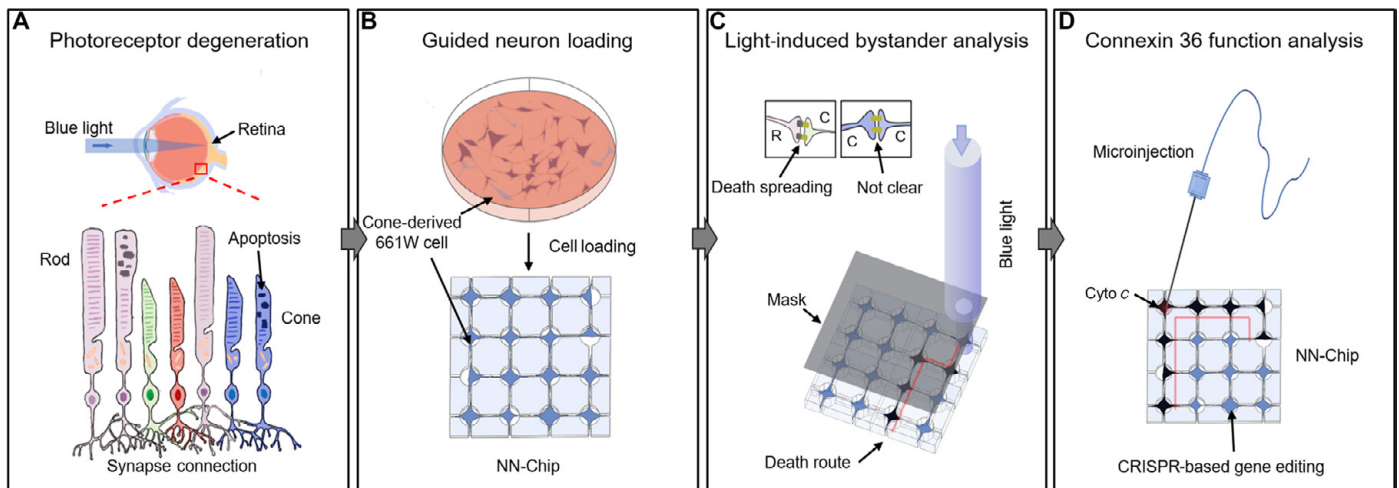


Fig. 1. Dissecting the mechanisms of photoreceptor degeneration via the bystander effect using the NN-Chip platform. (A) Excessive light irradiation induces apoptosis in photoreceptors, which are highly connected throughout the photoreceptor layer by random synapses. (B) To dissect photoreceptor communication, which is normally highly coupled in tissue and in dish culture, we loaded the 661W cells individually onto the NN-Chip. Each microwell was connected by microchannels to allow synapse formation between each photoreceptor, generating a highly guided neural network. (C) To study the bystander killing effect between cones, we selectively induced apoptosis using blue light sources. (D) To quantitatively analyze the role of Cx36 in bystander killing between cones on the NN-Chip, we used CRISPR (clustered regularly interspaced short palindromic repeats)-based gene-edited cells in conjunction with a microinjection unit.

(Fig. 1C). Using this clear and visualized system, we observed the apoptosis propagation between cones, which likely occurred due to the enhanced coupling via their connexin 36 (Cx36)-containing gap junctions (17). Next, to study the role of Cx36 in apoptosis, which is currently being debated (18, 19), and the bystander effect, we used a microinjection unit in conjunction with our NN-Chip platform to perform Cx36 loss-of-function studies (Fig. 1D). Our data showed that Cx36 is required for the cone-to-cone bystander killing phenomenon and is also a deterministic factor for the range and speed that apoptosis can spread. Our study suggests that this structural gap junction protein could be a potential treatment target for alleviating cone photoreceptor degeneration.

RESULTS

Design and operation of the NN-Chip platform

The NN-Chip was designed with AutoCAD software and fabricated using photolithography and polydimethylsiloxane (PDMS) technologies. The device is made up of 2.25×10^4 uniform microwells distributed as a 150×150 array, and all adjacent wells were connected by microchannels. In typical microfluidic devices, cells are trapped and loaded using fluid control, whereas in our NN-Chip, we placed suspended cells on top of the NN-Chip and then loaded single cells into each well using programmed centrifugation (Fig. 2, A and B, and movie S1). We designed our device as an up-open stage to facilitate various treatments on cell throughout the experiment, which is indispensable for the bystander effect research. To use the NN-Chip to assess the bystander effect between cones, the device parameters were empirically optimized to meet the following conditions: (i) Only one cell is loaded into each microwell. (ii) Cells should remain in the same well, without migration, during the entire experiment. (iii) Neurons spread their protrusions along with the channels and are coupled with adjacent cells (Fig. 2C). The NN-Chip can also load cells of different types and sizes by sequentially centrifuging into the corresponding wells, allowing the study of various combinations of cell interactions in the future.

For the cone photoreceptor-derived 661W cells, we found the optimal microwell diameter to be $20 \mu\text{m}$, the optimal channel width to be $3 \mu\text{m}$, and the length to be $20 \mu\text{m}$. To our knowledge, the NN-Chip has a higher cell-loading efficiency ($>95\%$ single-cell coverage) than single-cell microwell workstations used in previous reports (Fig. 2, D and E); moreover, this high-throughput platform is extremely suitable to study the bystander behavior (20). It should be noted that the arrayed pattern, the well diameter, and the channel width, length, and shape are required to be optimized for different cell types to achieve the highest loading efficiency (fig. S1). To prevent migration of the cultured cells, we coated Eagle's basal medium (BME) in the microwells and microchannels, but not on the rest of the chip surface (fig. S2). After the cells were loaded, they were incubated for 6 hours in the conditioned medium to promote attachment and synapse formation (Fig. 2, F and G, and movie S2). We also loaded iCell neurons onto the NN-Chip under another optimized condition. This induced pluripotent stem-derived primary neurons can create their uniform neural network with stable synapse coupling after culturing on the NN-Chip (Fig. 2H).

Finally, we equipped our NN-Chip platform with a high-resolution, multi-position microscope and a microinjection unit. This system permitted us to dissociate the complicated retina structure into a uniform network; moreover, the accompanying microinjection unit allowed chemical modification, and the high-resolution microscope enhanced our observation potential, thereby improving the ability to assess the bystander effect in photoreceptor degeneration.

Blue light irradiation-induced 661W cell apoptosis while culturing on the NN-Chip

Blue light induces more damage than other visible wavelengths in 661W cells (21). After blue light over-irradiation, excessive reactive oxygen species (ROS) are generated by the high level of oxidative stress, which induces damage to proteins, lipids, and DNAs and results in apoptosis (22, 23). On the basis of this knowledge, we measured ROS concentration after irradiation of the 661W-containing NN-Chip under a 3000-lux-intensity blue light source or a white light source with the same intensity

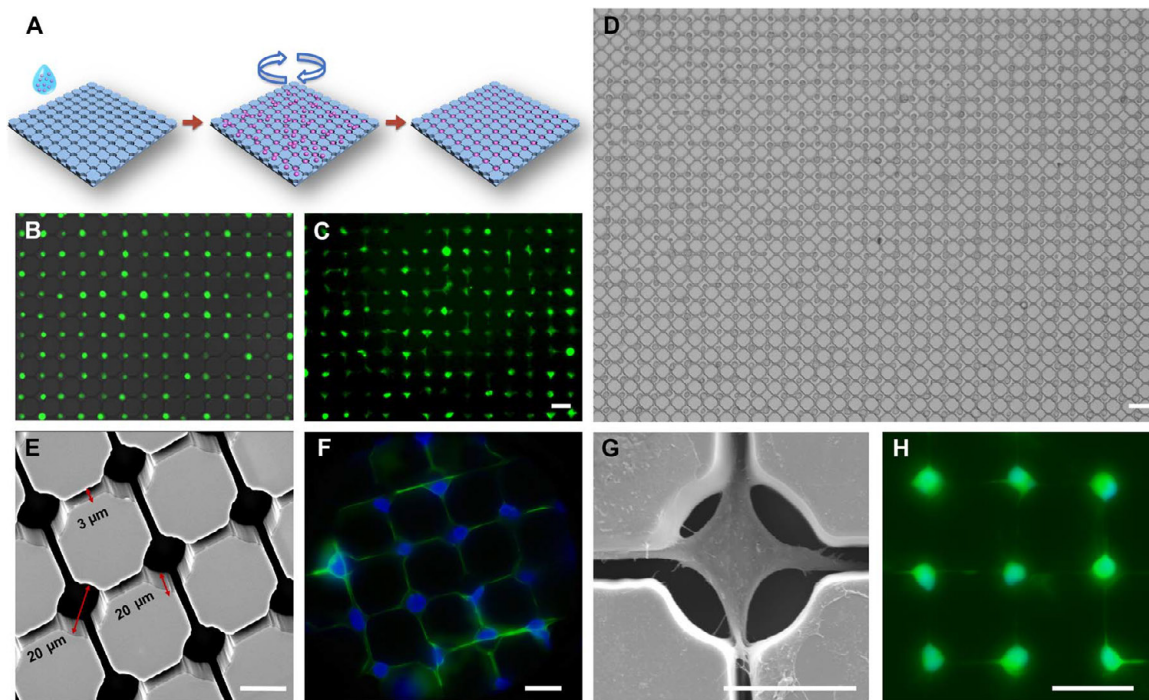


Fig. 2. Operation and design of the NN-Chip platform. (A) Schematic of the cell loading process. (B) Representative image of loading efficiency. The 661W cells were incubated in the medium with calcein for 20 min before loading. (C) Cell morphology after incubation for 1 hour on chip after loading. Scale bar, 40 μm . (D) Results of large-area loading by using the MDA-MB-231 cells with optimized parameters. Scale bar, 40 μm . (E) A scanning electron microscopy (SEM) image shows the neural network structure, including the microwells and their connecting microchannels, of the NN-Chip at a 30° tilt angle. (F) Representative images show that the 661W cells formed neural network on the NN-Chip. The actin (green) was labeled by phalloidin, and the nuclei (blue) was labeled with 4',6-diamidino-2-phenylindole (DAPI). (G) A representative SEM image shows a 661W cell with synapses extending into the surrounding chambers along with the microchannel. (H) Neural network created by iCell neurons. Cells were stained by calcein after culturing on chip for 12 hours. Scale bar, 20 μm .

as control for various times. Using a dichlorodihydrofluorescein diacetate (H_2DCFDA) ROS probe, we found that ROS concentration increased significantly after 6 hours of blue light irradiation compared with that of white light (control) treatment (Fig. 3A). After 24 hours of blue light irradiation, ROS accumulation decreased, likely because most of the cells were completely dysfunctional. It is possible that, in the 661W cells, continuous blue light absorption increases ROS accumulation to the levels that exceed the cells' antioxidative ability, thus triggering apoptosis. ROS accumulation has also been shown to reduce the mitochondrial membrane potential (mmp), which plays an essential role in the antioxidant defense system (24). Thus, we evaluated the mmp of blue light-treated 661W cells using the JC-1 mmp assay, which labels healthy cells (with high mmp) red, because of the JC-1 aggregates, and apoptotic cells (with low mmp) green, because of the JC-1 monomers. The cells with red and green signals (merged) were considered as pre-apoptotic (Fig. 3B and fig. S3). We also used SYTOX Green to stain the apoptotic cells to verify the existence of the light-sensitive characteristics in the 661W cells while culturing on the NN-Chip. According to statistical data, with increasing blue light irradiation, the number of pre-apoptotic and apoptotic 661W cells increased (Fig. 3, C and D). This assay also demonstrated that blue light irradiation, and the accompanying increased ROS production, resulted in a significant mmp reduction in the 661W cells.

Short-wavelength opsin (S-opsin) is a light-sensitive, cone photoreceptor-specific protein that is, not surprisingly, highly expressed in the 661W cells (25). Some researchers have noted the S-opsin aggregation as an indicator of cone photoreceptor dysfunction after blue

light irradiation (26). To determine whether this phenomenon occurs in our NN-Chip, we cultured the 661W cells on chip for 6 hours and then treated the cells with blue light for various times (fig. S4). S-opsin aggregation visibly increased after blue light treatment when compared with the white light group (Fig. 3E, arrows). Moreover, statistical results showed an increased percentage of S-opsin-aggregated cells in the 9- and 18-hour blue light-treated groups compared with those of the corresponding white light (Fig. 3F). Together, the increased ROS production, mitochondria dysfunction, and S-opsin aggregation that we observed after blue light irradiation demonstrated that the 661W cells, when cultured on our NN-Chip, maintain their previously documented light-sensitive properties; thus, the NN-Chip is a valid platform to study the bystander effect in the 661W cone photoreceptors.

Blue light-induced apoptosis spread to adjacent cells in a gap junction-dependent manner

To test the existence of bystander killing between cones, we first validated the existence of tight junctions in the connected synapses between adjacent 661W cells cultured on the NN-Chip (fig. S5). Then, a circular area with a radius of approximately 200 μm in the 661W-containing NN-Chip was treated for 6 hours using a 405-nm laser. After treatment, we removed the laser and monitored the apoptotic cell distribution by SYTOX Green staining. We monitored the results for up to 24 hours after irradiation, and it appeared that apoptosis had spread from the irradiated area to the adjacent cells. To determine whether apoptosis signals are transported to the adjacent cells via gap junctions, we added the gap junction blocker octanol (1 mM) to the culture medium (27);

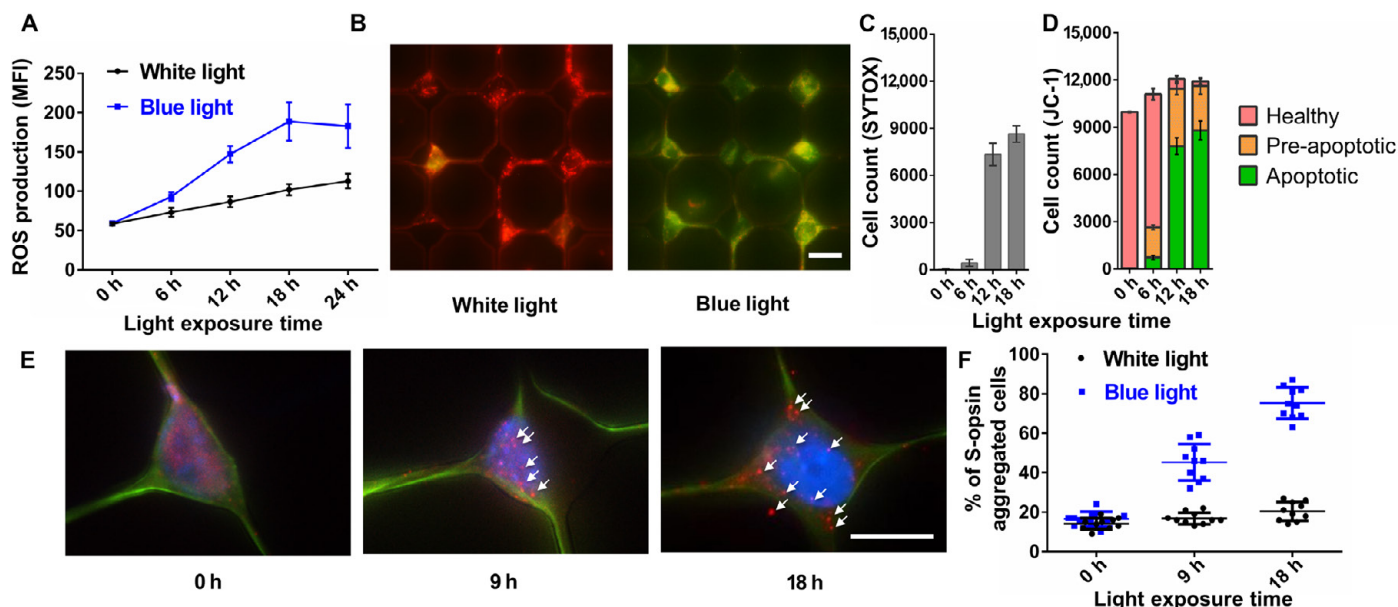


Fig. 3. Maintaining the blue light-sensitive characters of 661W cells after loading and culturing on the NN-Chip. (A) ROS production accumulation, as measured by the mean fluorescence intensity (MFI) of H_2DCFDA , was assessed following blue or white light irradiation for various times ($n = 10$). (B) Representative images show JC-1-stained 661W cells after blue light irradiation. The healthy cells with high mmp appeared red (aggregates), the apoptotic cells with low mmp appeared green (monomers), and the pre-apoptotic cells appeared red and green. Scale bar, 20 μm . (C) Number of the SYTOX Green-labeled cells under blue light irradiation for different time intervals. (D) Percentage of cells in each JC-1-stained group, which were counted in a 100×100 cell array ($n = 10$). (E) Representative immunostaining images show S-opsin aggregation in 661W cells on the NN-Chip after blue light irradiation for 9 and 18 hours. The cells were stained for actin [green fluorescent protein (GFP)] and S-opsin (Alexa Flour 647), and the nuclei were stained with DAPI. Scale bar, 20 μm . (F) Quantitative analysis showed that the percentage of S-opsin-aggregated cells was increased by blue light irradiation compared with that by white light irradiation.

this treatment appeared to ameliorate the spread of apoptosis during the 24-hour post-irradiation window. We also used quinine (50 μM) and meclofenamic (100 μM), which can selectively inhibit Cx36 and Cx43 individually to test the functions of different connexin types during the apoptosis propagation (28–30). Quinine also blocked apoptosis spreading, but meclofenamic did not. These results showed that, in cone photoreceptors, Cx36 plays a vital role in controlling apoptosis spreading, but Cx43 only slightly affects this phenomenon (Fig. 4A). We counted the apoptotic cells every hour after irradiation in each group. In the nontreated group, apoptosis increased throughout the time course; however, this increase was inhibited in the octanol- and quinine-treated group (Fig. 4B and movie S3). Together, all these data provided convincing evidence for the existence of a gap junction-dependent bystander killing effect manner between cone photoreceptors. In addition, Cx36, mainly expressed in the central neuron system especially in cones, could be a potential target for preventing the apoptosis spreading.

To assess the bystander killing effect at the single-cell level, we used a photomask with 1000 5- μm -radius transparent pinholes on top of the NN-Chip, which only allows blue light irradiation on only one cell each time. We first recorded the positions of the apoptotic cells after blue light irradiation. After that, we monitored the apoptotic cell distribution for various times and quantified the number of the post-apoptotic cells adjacent to the original ones. Time-lapse microscopy revealed that apoptosis eventually occurred in cells adjacent to the blue light-treated cells (Fig. 5A and movie S4). Next, we quantified the apoptotic cell distribution across the NN-Chip after blue light irradiation. We found that 80% of the subsequent apoptotic cells were adjacent to the originally treated ones, whereas the remaining apoptotic cells seemed to reflect as

random apoptotic behavior (fig. S6). To further address the mechanism, we hypothesized that, if apoptosis spreads via paracrine, the apoptotic cells should be distributed uniformly around the blue light-treated cells, whereas if apoptosis spreads via gap junctions, the apoptotic cells should be distributed asymmetrically. To distinguish between these two scenarios, we counted the number of post-apoptotic cells adjacent to each pretreated cell. Most pretreated cells were only adjacent to one or two apoptotic cells (Fig. 5B), implying that apoptosis propagation is occurring directionally, likely via gap junctions, and not uniformly as paracrine. Finally, these results demonstrated the existence of the bystander killing effect in cone-derived 661W photoreceptors. Because cones are critical for color recognition and high visual acuity (31), treatments that inhibit this gap junction-mediated bystander effect between cones could extend the visual capabilities in some retinal disease patients with cone photoreceptor degeneration.

Cx36 is required for apoptosis spreading in cone photoreceptors

Gap junctions allow the passage of substances less than 1 kDa, such as Ca^{2+} , inositol triphosphate, and adenosine triphosphate; however, the exact role of the gap junction protein Cx36 in the cone bystander killing effect remains controversial (9, 17–19, 32–34). On the basis of our results that Cx36 may have crucial functions in death signal transportation in cones, we then targeted this gap junction using a more straightforward method: by knocking out Cx36 in the 661W cells (Fig. 6A and fig. S7). Next, we used a microinjection unit to inject cytochrome c into single Cx36-knockout (KO) and wild-type (WT) 661W cells cultured on the NN-Chip to measure the apoptosis spreading results. In the cytoplasm, with the release of cytochrome c, several downstream apoptotic signals

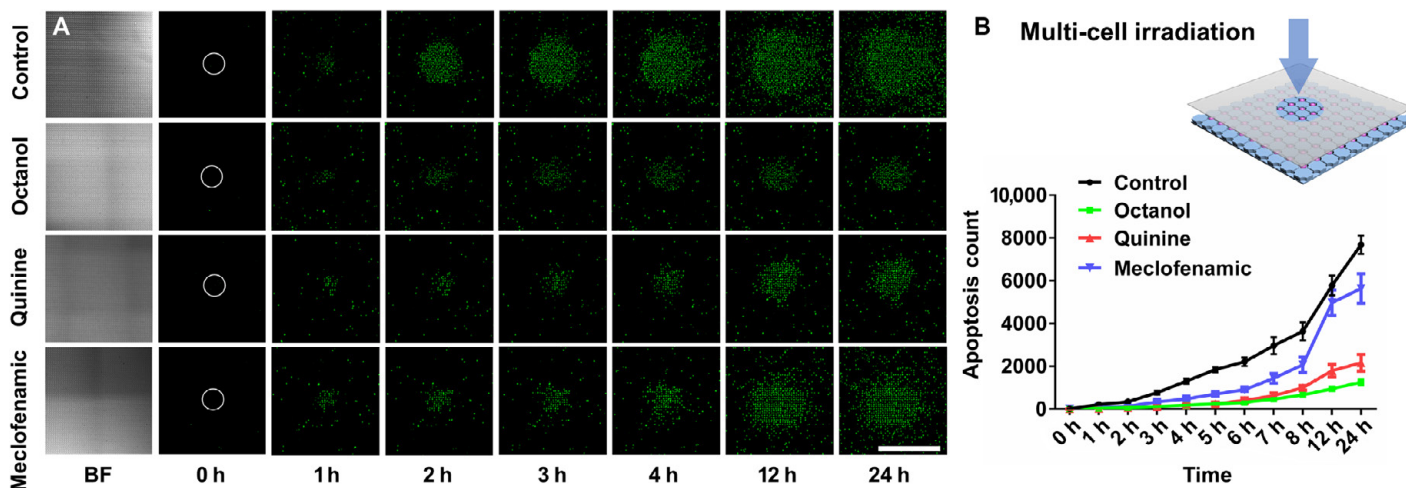


Fig. 4. Evidence of the gap junction–mediated bystander killing effect in the 661W cells. (A) Representative bright field (BF) and fluorescence images show apoptosis distribution, detected by SYTOX staining, in different gap junction inhibitors (octanol, 1 mM; quinine, 50 μ M; meclofenamic, 100 μ M) after 6 hours of blue light irradiation on the 661W-containing NN-Chip. White circles represent the initial irradiated area. Scale bar, 1 mm. (B) Schematic of the 405- μ m laser spot diameter irradiation of the NN-Chip. Apoptosis was counted every hour for 24 hours after blue light irradiation ($n = 10$).

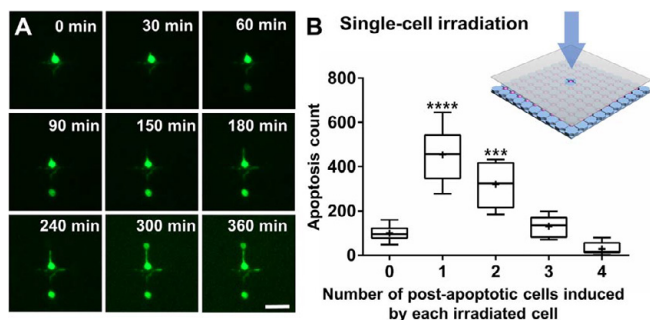


Fig. 5. Analysis of the bystander killing phenomenon at the single-cell level. (A) Representative time-course images of the bystander effect at the single-cell level in SYTOX-stained 661W cells on the NN-Chip. A single cell was irradiated to blue light, and two adjacent cells eventually undergo apoptosis. Scale bar, 40 μ m. (B) Schematic of the 5- μ m laser spot irradiation of the NN-Chip. The number of post-apoptotic cells induced by each pretreated cell was quantified. The whiskers go down to the smallest value and up to the largest. $P < 0.0001$ by one-way analysis of variance (ANOVA) analysis compared with zero- and four-cell group; $n = 10$.

are activated. Compared with light irradiation, both methods can trigger cell apoptosis, but cytochrome *c* acts as a more direct factor (35). Therefore, we chose the microinjection of cytochrome *c*, instead of light irradiation, to standardize the apoptosis time at the single-cell level.

Before performing the cytochrome *c* microinjection experiments, we optimized the experimental parameters. First, to minimize cell damage and satisfy that cells can still keep their normal function after injection, we optimized the injection pressure to 60 hPa, compensation pressure to 30 hPa, and injection time to 0.1 s (Fig. 6B and fig. S8) (36). Next, because only substances less than 1 kDa can pass through gap junctions, we verified gap junction function in our 661W-containing NN-Chip by injecting tracers of different molecular weights and monitoring their spread into adjacent cells. We injected solutions containing 100 mM Lucifer yellow (457 Da) and 100 mM fluorescein isothiocyanate (FITC)–dextran (10 kDa), and then analyzed their spreading after 15 min. Lucifer yellow, but not FITC–dextran, easily passed through the gap junctions into adjacent cells (Fig. 6, C and D). Similarly, after

injection of both Lucifer yellow and Cascade blue dextran (3 kDa) into the same cell, Lucifer yellow, but not blue dextran, was observed in adjacent cells (Fig. 6, E and F). These data suggest that the gap junctions are functional between the 661W cells on the NN-Chip. These results are consistent with previous reports that showed that only substances less than 1 kDa can pass through the gap junctions (37).

After optimization, we mixed cytochrome *c* (10 mg/ml) and blue dextran (20 mg/ml) in microinjection buffer and injected it into the Cx36-KO and WT 661W cells; after 30 min, we cultured them in the SYTOX Green–containing medium. After 6 hours, we assessed the apoptosis and dextran spreading results. The Cx36-KO cells showed visibly less cell apoptosis spreading compared with the WT cells, and the dextran spreading patterns were similar to those of SYTOX in both groups (Fig. 6, G to J). In addition to the gap junctions remaining open after cell apoptosis, the gap junctions may be dysfunctional because of the loss of membrane integration during the bystander killing process, leading the blue dextran spread to the adjacent cells to form this similar pattern (38, 39). Finally, we quantified apoptosis in cells adjacent to the cytochrome *c*–microinjected cells and demonstrated that the injected Cx36-KO cells had fewer adjacent cells undergoing apoptosis than the injected WT cells (Fig. 6K). These data suggest that Cx36 is responsible for the gap junction–dependent bystander effect in cone photoreceptors.

In summary, although inhibition of Cx36 may relieve the bystander effect in retinal diseases, Cx36 also provides many important functions in the retinal system (32, 33, 40), making it difficult to completely block Cx36 as a retinal protection mechanism (41). Thus, in the future, we aim to elucidate the importance rank of specific death signals, such as ion and microRNAs involved in the bystander effect, using the NN-Chip combined with the microinjection technologies; this should reveal a more feasible method to remedy cone photoreceptor degeneration.

DISCUSSION

Considerable research efforts have focused on finding the molecular mechanisms underlying the bystander effect, with most studies focusing on the role of connexins and gap junctions. Treating cells and observing

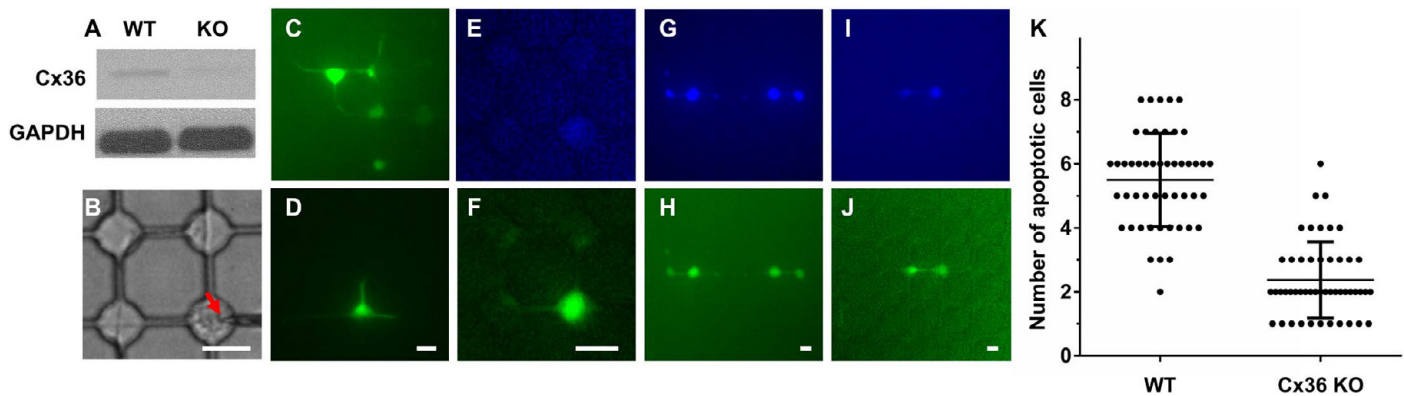


Fig. 6. Assessing the effects of Cx36 on apoptosis spreading in the 661W cells. (A) Western blot analysis shows loss of Cx36 in Cx36-KO cells relative to that in WT cells. Glyceraldehyde-3-phosphate dehydrogenase (GAPDH) was used as a loading control. (B) A cell was being injected with a Femtotip (inner diameter, 0.5 μm ; outer diameter, 1 μm ; Eppendorf) on the NN-Chip. (C and D) Dye distribution in 15 min after injection of 100 mM Lucifer yellow (457 Da) in (C) or of 100 mM FITC-dextran (10 kDa) in (D). (E and F) Dye distribution in 15 min after the injection of blue dextran (3 kDa) (E) and Lucifer yellow (F) and into the same cell. (G and H) Representative images show blue dextran (G) and SYTOX (H) distribution 6 hours after cytochrome c (10 mg/ml) and blue dextran (20 mg/ml) co-injection into a single WT cell. (I and J) Representative images show blue dextran (I) and SYTOX (J) distribution 6 hours after cytochrome c (10 mg/ml) and blue dextran (20 mg/ml) co-injection into a single Cx36-KO cell. (K) Quantitative analysis of apoptosis in WT and Cx36-KO groups. The results are calculated from 50 single-cell injections per group. Scale bars, 20 μm (B to J).

the behavior of adjacent cells have been the general methods used to dissect the mechanism of the bystander effect. However, researching the bystander killing effect at the single-cell level is a more recent trend that can uncover biological signals without the influence of uncertain elements associated with the complex structure and organization of neural networks. To date, photoreceptor bystander research is fraught with technical challenges, including difficulties in dissociating retinal structures and quantitatively measuring bystander killing speed, unclear observations, and the lack of a reliable single-cell assay. Thus, the ability to observe and quantify the bystander killing effect in cone photoreceptors is instrumental for further mechanistic research.

Here, we developed an innovative NN-Chip platform capable of high-efficiency cell loading via a user-friendly centrifugation method, allowing the immobilization of single cells in individual microwells; the cells are connected to adjacent cells via synapses at uniform distances. Furthermore, because our NN-Chip is an up-open platform combined with a microinjection unit, we can quickly treat single cells and assess the effects on adjacent ones. Using this platform, we demonstrated several findings regarding the bystander effect in cone photoreceptors. First, we established the existence of the bystander killing effect between cone photoreceptor-derived 661W cells by showing that blue light-induced apoptosis in one cell can directionally spread to adjacent cells. In our opinion, we have provided strong, clear, and, most importantly, quantitative evidence of a cone-to-cone bystander killing phenomenon. Second, we assessed the role of the gap junction protein Cx36, which is highly expressed in cones as a communication channel, in bystander killing phenomenon. Disruption of Cx36 via CRISPR-Cas9 (CRISPR-associated protein 9 nuclease) gene editing greatly decreased the apoptosis spreading compared with that of WT 661W cells. These data suggest that, in the cone photoreceptor layer, Cx36-containing channels act as tunnels that allow the passage of apoptotic signals between cone photoreceptors, thus propagating apoptosis throughout the entire photoreceptor layer.

In retina degeneration diseases, the bystander effect is an established mechanism to dissect apoptosis propagation from dying cells to healthy neighbors (4). As researches show, the gap junction provides a transmitting channel for toxic substances from dying rods to healthy cones (10), and we consequently analyzed the secondary bystander effect between

cones. On the basis of our results that Cx36 provides an avenue for toxic spreading, we may conclude that, although the Cx36-based GJIC is not the only method between cones, Cx36 truly regulates the transmission of toxicity elements. Recently, the use of gene therapies and combined approaches has provided promising therapeutic perspectives; thus, Cx36 may provide a potential treatment target to delay the spreading of photoreceptor degeneration.

In conclusion, we created a novel platform for high-efficiency patterning of neural networks, combined with a microinjection unit, which we believe will lessen the challenges for dissecting the mechanisms of the bystander effect and gap junction functions. Moreover, this platform should have additional applications in other types of neuron studies.

MATERIALS AND METHODS

Cell culture

The 661W photoreceptor cell line was provided by M. Al-Ubaidi (Department of Biomedical Engineering, University of Houston). These cells were routinely cultured in Dulbecco's modified Eagle's medium (Gibco) supplemented with 10% heat-inactivated fetal bovine serum (Thermo Fisher Scientific) and 1% antibiotic-antimycotic (Gibco, 15240-062) with hydrocortisone 21-hemisuccinate (40 ng/ml; Sigma, H-2270), progesterone (40 ng/ml; Sigma, P-8783), putrescine (0.032 mg/ml; Sigma, P-7505), and 0.004% (v/v) β -mercaptoethanol (Sigma, M-6250) at 37°C in a humidified atmosphere with 5% CO_2 . We used the conditioned medium (medium cultured with 661W cells for 6 hours) to culture cells on BME (Sigma)-coated NN-Chips. We cultured the iCell neurons (Cellular Dynamics International Inc.) onto the poly-L-ornithine/laminin (Sigma) surface-coated NN-Chip in the complete iCell neuron maintenance medium also at 37°C in a humidified atmosphere with 5% CO_2 .

Design and fabrication of the NN-Chip mold

All designs were drawn with AutoCAD software and loaded as glass photomasks (Photo Sciences Inc.). PDMS devices were fabricated by standard photolithography and elastomer molding. We used SU-8 3025 negative photoresist (MicroChem Corp.) to fabricate the 20- μm -deep structures. The SU-8 3025 photoresist was spin-coated onto a 12.7-cm

silicon wafer at 500 rpm (Laurell Technologies Corp., model WS-400B-6NPP/LITE/AS) for 10 s with an acceleration of 100 rpm/s to spread out the photoresist and then at 3500 rpm for 60 s with an acceleration of 500 rpm/s. After soft baking at 65°C for 3 min and hard baking at 95°C for 10 min, the wafer was exposed under ultraviolet light with an exposure dose of 150 mJ/cm² for 3 s. It was then heated for post-exposure baking at 65°C for 1 min and hard baking at 95°C for 3 min. After 135°C heating for 30 min, the wafer was hydrophobic-processed by trimethylchlorosilane for 30 min. The modified wafer served as an SU-8 mold structure. The PDMS oligomer and cross-linking pre-polymer of the PDMS agent from a Sylgard 184 kit (Dow Corning) were mixed in a weight ratio of 10:1. After degassing in vacuum, the appropriate weight mixture was poured onto the SU-8 mold to form a 2-mm-thick layer and cured at 85°C for 40 min. After the PDMS replica was peeled off from the SU-8 mold, we cut the PDMS into several 6 × 6 mm squares. For better imaging and cell culturing method, we bonded the PDMS flat surface side to 12-mm glass-based 35-mm dish (Thermo Fisher Scientific) by oxygen plasma [1 min at an oxygen flow rate of 20 SCCM (standard cubic centimeter per minute), a chamber pressure of 500 mtorr, and a power of 50 W].

Operation of the NN-Chip

To load cells into the NN-Chip, we used the Sorvall Legend X1R Centrifuge (Thermo Fisher Scientific). First, we treated the NN-Chip surface by oxygen plasma (1 min at an oxygen flow rate of 20 SCCM, a chamber pressure of 500 mtorr, and a power of 50 W), immediately covered it with a BME droplet, and placed it at 37°C for 1 hour. After coating, we swiped the excessive liquid and moved the surface onto a 95°C digital dry bath (Bio-Rad) for 1 s to denature the BME coated on the surface. Once finished, we used a Staples invisible tape to peel off the excessive BME. After surface modification, we dropped the 20- μ l medium containing suspended cells onto the surface of NN-Chip. We tested several spinning modes and chose the programmed centrifugation as follows: (i) 0 to 1000 rpm, acceleration = 1; (ii) 1000 rpm for 1 min; (iii) 1000 to 600 rpm, deceleration = 1; (iv) 600 to 0 rpm, deceleration = 9. After spinning, we transferred the NN-Chip to an inverted microscope (EVOS) and used filter papers (Whatman) from one side to swipe away the unloaded cells. Finally, we slightly dropped the 20- μ l conditioned medium on the NN-Chip and cultured cells at 37°C in a humidified atmosphere with 5% CO₂. All the operations were finished in a culture hood to prevent contamination.

Creating the cone photoreceptor network

Loading single 661W cells with high efficiency is crucial for this high-throughput, single neural network platform. Correctly sizing the wells to match the 661W cell size largely influenced the loading efficiency. Efficiency improved as the well diameters increased from 20 to 30 μ m; however, well diameters >30 μ m increased the chance of two-cell loading. The density of the suspended cells also affected the loading efficiency, which was decreased by low density and cell gathering. Finally, we optimized the distance between the 661W cells to ensure high coupling of their synapses. We found that 40 μ m between the center of every well was the optimal distance to ensure synapse coupling, without large-cell membrane contact. After all these optimizations, we routinely obtained a loading efficiency of >95%.

Cell staining

To have a better image, we used calcein (Thermo Fisher Scientific) to stain live cells. Cells were cultured in the calcein-containing medium

(1 μ M) for 30 min and then loaded onto the NN-Chip. Stained cells can keep the fluorescence for around 1 hour (fig. S1). We also used phalloidin (A12379, Invitrogen) to label the actin in the 661W cells.

Light treatment to the 661W cells

We used two kinds of blue and white light sources to treat cells under 3000-lux-intensity conditions. Cells were first loaded onto the NN-Chip and incubated under a humidified atmosphere of 5% CO₂ at 37°C. Then, they were treated with blue light-emitting diode (LED; 464 nm) or laser diode (405 nm) light on top of the NN-Chip, and the intensities were adjusted to the same lux using the Extech LT300 light meter (FLIR Commercial Systems Inc.). Control cells were incubated under the same intensity white LED light (the wavelength peaks are 456 and 553 nm) with the same humidity and temperature environment.

Measurement of cellular ROS production and mmp

For ROS production measurements, 661W cells were loaded onto the NN-Chip and cultured for 6 hours. After 6, 12, 18, or 24 hours of blue or white light irradiation, we added 10 μ M CM-H₂DCFDA (Invitrogen) to the culture medium and incubated for an additional hour. CM-H₂DCFDA fluorescence was measured using a microplate reader (M33089, Thermo Fisher Scientific). Mmp was measured after the 661W cells were exposed to blue light for 6, 12, or 18 hours using the JC-1 Mitochondrial Membrane Potential Assay Kit (ab11850, Abcam). The images were captured using a fluorescence microscope (EVOS FL Auto Cell Imaging System), and the numbers of fluorescent cells (red, green, and merged) were counted using ImageJ.

Immunostaining

The 661W cells were loaded onto the NN-Chip and incubated for various times. For S-opsin immunostaining, we fixed the cells with 4% paraformaldehyde (Sigma) for 10 min and blocked them in 3% bovine serum albumin (Sigma) for 30 min after blue light irradiation. Then, we incubated the fixed cells overnight at 4°C with the primary antibody (sc-14363, Santa Cruz Biotechnology Inc.). After washing, the cells were incubated for 1 hour with the secondary antibody [donkey anti-goat immunoglobulin G (IgG) H&L (Alexa Fluor 647), Abcam]; then, cell nuclei were stained with DAPI. For Cx36 immunostaining, we used the same procedure with the following antibodies: Cx36 polyclonal antibody (Invitrogen), claudin-1 polyclonal antibody (Invitrogen, 71-7800), and goat anti-rabbit IgG H&L (Alexa Fluor 647, Abcam). Images were taken using a Nikon A1 confocal microscope.

Cell apoptosis analysis

SYTOX Green Dead Cell Stain (Thermo Fisher Scientific) was used to measure apoptosis levels in 661W cells. Medium containing SYTOX (0.5 μ M) was added to the NN-Chip after blue light treatment to stain the nucleotides of dead cells; then, we observed apoptosis spreading by time-lapse microscope. To verify the SYTOX results, we used the Annexin V-FITC Apoptosis Detection Kit (Abcam) per the manufacturer's instructions. Dead cells were counted using ImageJ.

Generation of Cx36-KO 661W cells

The 661W cells were cultured in six-well plates at a density of 5 × 10⁴ cells per well for 24 hours. Then, we added 2 μ g of CRISPR/Cas9-Cx36-KO plasmid with a GFP reporter (sc-420563, Santa Cruz Biotechnology) and 6 μ l of FuGENE HD Transfection Reagent (Promega) complex to 100 μ l of Opti-MEM (Gibco). This transfection reaction was added to the culture medium, and after 24-hour incubation, we sorted the GFP-expressing

cells by flow cytometry (LSRFortessa, BD Biosciences). Then, we expanded these cells as single-cell colonies to screen for Cx36-KO 661W cells.

Western blotting analysis

The control and Cx36-KO 661W cells were seeded at a density of 5×10^5 cells per well in six-well plates and incubated for 24 hours. Then, the cells were washed with phosphate-buffered saline, lysed in radioimmunoprecipitation assay buffer (Sigma), and harvested. Lysates were centrifuged at 12,000 rpm for 10 min at 4°C. The protein concentrations were measured using the BCA Protein Assay Kit (Thermo Fisher Scientific) with standard bovine serum albumin. The samples were boiled for 10 min at 100°C. The proteins were separated by SDS-polyacrylamide gel electrophoresis gradient electrophoresis and transferred to polyvinylidene difluoride membranes (Bio-Rad). We used goat anti-Cx36 (sc-14904, Santa Cruz Biotechnology) as the primary antibody and horseradish peroxidase-conjugated donkey anti-goat IgG (ab97110, Abcam) as the secondary antibody.

Operation of microinjection system

The microinjection system included a microinjector (FemtoJet 4i, Eppendorf) and a micro-manipulator (MS314, WPI) at a step resolution of 0.5 μm . Injected liquid was loaded with a micro-loader (Eppendorf) and then injected into the cells. All the injection process was observed under a charge-coupled device camera (C11440, Hamamatsu), which was a part of the Nikon eclipse Ti-based N-STORM microscopy system.

REFERENCES AND NOTES

- A. F. Wright, C. F. Chakarova, M. M. A. El-Aziz, S. S. Bhattacharya, *Nat. Rev. Genet.* **11**, 273–284 (2010).
- A. B. Belousov, J. D. Fontes, *Neural Regen. Res.* **11**, 75–76 (2016).
- E. Decrock *et al.*, *Cell Death Differ.* **16**, 524–536 (2009).
- H. Ripps, *Exp. Eye Res.* **74**, 327–336 (2002).
- K. Cusato *et al.*, *J. Neurosci.* **23**, 6413–6422 (2003).
- P. Kameritsch, N. Khandoga, U. Pohl, K. Pogoda, *Cell Death Dis.* **4**, e584 (2013).
- C. L. Cepko, *Annu. Rev. Vis. Sci.* **1**, 211–234 (2015).
- S. Kohl *et al.*, *Nat. Genet.* **19**, 257–259 (1998).
- D. C. Spray *et al.*, *Wiley Interdiscip. Rev. Membr. Transp. Signal.* **2**, 1–15 (2013).
- W. Zhang *et al.*, *Proc. Natl. Acad. Sci. U.S.A.* **109**, 18707–18712 (2012).
- K. Zhang, C.-K. Chou, X. Xia, M.-C. Hung, L. Qin, *Proc. Natl. Acad. Sci. U.S.A.* **111**, 2948–2953 (2014).
- N. Chronis, M. Zimmer, C. I. Bargmann, *Nat. Methods* **4**, 727–731 (2007).
- J. W. Park, B. Vahidi, A. M. Taylor, S. W. Rhee, N. L. Jeon, *Nat. Protoc.* **1**, 2128–2136 (2006).
- E. Tan *et al.*, *Invest. Ophthalmol. Vis. Sci.* **45**, 764–768 (2004).
- M. Rapp, G. Woo, M. R. Al-Ubaidi, S. P. Becerra, P. Subramanian, in *Retinal Degenerative Diseases* (Springer, 2014), pp. 813–820.
- L.-p. Yang, X.-. Zhu, M. O. M. Tso, *Invest. Ophthalmol. Vis. Sci.* **48**, 4766–4776 (2007).
- J. J. O'Brien, X. Chen, P. R. MacLeish, J. O'Brien, S. C. Massey, *J. Neurosci.* **32**, 4675–4687 (2012).
- A. B. Belousov, J. D. Fontes, *Trends Neurosci.* **36**, 227–236 (2013).
- J. C. de Rivero Vaccari, R. A. Corriveau, A. B. Belousov, *J. Neurophysiol.* **98**, 2878–2886 (2007).
- J. R. Rettig, A. Folch, *Anal. Chem.* **77**, 5628–5634 (2005).
- L. M. Rapp, S. C. Smith, *Invest. Ophthalmol. Vis. Sci.* **33**, 3367–3377 (1992).
- E. I. Azzam, S. M. de Toledo, J. B. Little, *Oncogene* **22**, 7050–7057 (2003).
- Y. Kuse, K. Ogawa, K. Tsuruma, M. Shimazawa, H. Hara, *Sci. Rep.* **4**, 5223 (2014).
- S. G. Jarrett, M. E. Boulton, *Mol. Aspects Med.* **33**, 399–417 (2012).
- P. H. Tang, M. C. Buhusi, J.-X. Ma, R. K. Crouch, *J. Neurosci.* **31**, 18618–18626 (2011).
- T. Zhang, N. Zhang, W. Baehr, Y. Fu, *Proc. Natl. Acad. Sci. U.S.A.* **108**, 8879–8884 (2011).
- G. R. Juszcak, A. H. Swiergiel, *Prog. Neuropsychopharmacol. Biol. Psychiatry* **33**, 181–198 (2009).
- M. Srinivas, M. G. Hopperstad, D. C. Spray, *Proc. Natl. Acad. Sci. U.S.A.* **98**, 10942–10947 (2001).
- E. G. A. Harks *et al.*, *J. Pharmacol. Exp. Ther.* **298**, 1033–1041 (2001).
- M. Srinivas, D. C. Spray, *Mol. Pharmacol.* **63**, 1389–1397 (2003).
- E.-J. Lee *et al.*, *Eur. J. Neurosci.* **18**, 2925–2934 (2003).
- B. Teubner *et al.*, *J. Membr. Biol.* **176**, 249–262 (2000).
- A. Calabrese *et al.*, *Diabetes* **52**, 417–424 (2003).
- J. Rash *et al.*, *Proc. Natl. Acad. Sci. U.S.A.* **97**, 7573–7578 (2000).
- A. J. Kole, E. R. Knight, M. Deshmukh, *J. Vis. Exp.* **52**, e2773 (2011).
- R. N. Cottle, C. M. Lee, D. Archer, G. Bao, *Sci. Rep.* **5**, 16031 (2015).
- S. A. Bloomfield, B. Völgyi, *Nat. Rev. Neurosci.* **10**, 495–506 (2009).
- K. Cusato, H. Ripps, J. Zakevicius, D. Spray, *Cell Death Differ.* **13**, 1707–1714 (2006).
- J. C. Goldstein, N. J. Waterhouse, P. Juin, G. I. Evan, D. R. Green, *Nat. Cell Biol.* **2**, 156–162 (2000).
- V. Gomez-Vicente, M. Donovan, T. Cotter, *Cell Death Differ.* **12**, 796–804 (2005).
- A. Akopian *et al.*, *J. Neurosci.* **34**, 10582–10591 (2014).

Acknowledgments: We thank M. Al-Ubaidi from the University of Houston for providing the 661W cells. **Funding:** We are grateful for funding support from R01 CA180083, R56 AG049714, and R21 CA191179. **Author contributions:** Y.M., X.H., and L.Q. designed research; Y.M., X.H., and B.C.C. performed research; Y.M., B.C.C., P.Z., and K.Z. analyzed data; Y.M., B.C.C., Z.H., and L.Q. wrote the paper. **Competing interests:** The authors declare that they have no competing interests. **Data and materials availability:** All data needed to evaluate the conclusions in the paper are present in the paper and or the Supplementary Materials. Additional data related to this paper may be requested from the authors. The 661W cell can be provided by M. Al-Ubaidi from the University of Houston pending scientific review and a completed materials transfer agreement. Requests for the 661W cell should be submitted to M. Al-Ubaidi.

Submitted 10 January 2018

Accepted 21 March 2018

Published 9 May 2018

10.1126/sciadv.aas9274

Citation: Y. Ma, X. Han, R. B. de Castro, P. Zhang, K. Zhang, Z. Hu, L. Qin, Analysis of the bystander effect in cone photoreceptors via a guided neural network platform. *Sci. Adv.* **4**, eaas9274 (2018).

SUPPLEMENTARY MATERIALS

Supplementary material for this article is available at <http://advances.sciencemag.org/cgi/content/full/4/5/eaas9274/DC1>

fig. S1. Optimization of the parameters and conditions for high-efficiency 661W cell loading.

fig. S2. A schematic shows the microwell BME-coating process on the NN-Chip.

fig. S3. ROS production, mmp measurements, and SYTOX function test in the blue light-treated 661W cells.

fig. S4. Representative immunostaining images of S-opsin from 0 to 18 hours under blue light irradiation.

fig. S5. Existence of tight junctions in synapses and function validation of the SYTOX.

fig. S6. Apoptotic cells were quantified with or without adjacent apoptotic cells ($n = 10$).

fig. S7. Generation and verification of Cx36-KO 661W cells.

fig. S8. Calibration of the microinjection volume.

movie S1. Operation of NN-Chip.

movie S2. Three-dimensional structural view of 661W cells cultured onto NN-Chip after 6 hours.

movie S3. Time lapse of the gap junction-mediated bystander killing effect in the 661W cells.

movie S4. Apoptosis propagation from single cell.

BIOPHYSICS

Bacteria as living patchy colloids: Phenotypic heterogeneity in surface adhesion

Teun Vissers,^{1*} Aidan T. Brown,¹ Nick Koumakis,¹ Angela Dawson,¹ Michiel Hermes,^{1,2} Jana Schwarz-Linek,¹ Andrew B. Schofield,¹ Joseph M. French,^{1,3} Vasileios Koutsos,³ Jochen Arlt,¹ Vincent A. Martinez,¹ Wilson C. K. Poon¹

Understanding and controlling the surface adhesion of pathogenic bacteria is of urgent biomedical importance. However, many aspects of this process remain unclear (for example, microscopic details of the initial adhesion and possible variations between individual cells). Using a new high-throughput method, we identify and follow many single cells within a clonal population of *Escherichia coli* near a glass surface. We find strong phenotypic heterogeneities: A fraction of the cells remain in the free (planktonic) state, whereas others adhere with an adhesion strength that itself exhibits phenotypic heterogeneity. We explain our observations using a patchy colloid model; cells bind with localized, adhesive patches, and the strength of adhesion is determined by the number of patches: Nonadherers have no patches, weak adherers bind with a single patch only, and strong adherers bind via a single or multiple patches. We discuss possible implications of our results for controlling bacterial adhesion in biomedical and other applications.

INTRODUCTION

Bacterial colonization of myriad niches, both natural and man-made, begins with adhesion to surfaces (1, 2). The colonization of man-made surfaces (catheters, surgical implants, etc.) causes infection (3) because adhering biofilms resist physical and chemical assaults (4), and it contributes to the emergence of antimicrobial resistance (5). Understanding and minimizing bacterial adhesion is a cross-disciplinary “grand challenge” (6), in which it is key to understand the forces involved. Besides generic electrostatics and dispersion forces (7), there are also forces of biological origin associated with various adhesins and sticky organelles (for example, fimbriae) (6, 8–10).

Biophysical studies of bacterial adhesion typically fall into two categories (11): high-throughput, population-level work giving little single-cell information or low-throughput single-cell studies. We report a robust, generic, and high-throughput tracking and big-data analysis technique that reveals detailed single-cell information in a large population. Applying this technique to *Escherichia coli* on glass, we find substantial variability in the propensity for adhesion and the postadhesion dynamics. Some cells do not adhere despite repeated encounters, whereas others adhere rapidly upon contact. Among the adherers, a fraction pivot freely around their own attachment points and can be removed from the surface by gravity, whereas the remainder spend part of their time in a more strongly bound, rotationally constrained state. This variability remains in flagella- and fimbriae-deletion mutants.

From the biological perspective, such variability exemplifies phenotypic heterogeneity in a clonal population (12) and offers a new model for its study (13, 14). Given the variety of surfaces that bacteria may encounter, such adhesive phenotypic heterogeneity may be an instance of “bet hedging” (15), allowing survival when the environment changes unpredictably (for example, following fecal excretion for Enterobacteriaceae).

In soft matter terms, genetically monodisperse *E. coli* cells are adhesively polydisperse and behave as “living patchy colloids” bearing a

variable number of sticky patches on their cell bodies. Thus, the considerable knowledge about patchy colloids accumulated over the past decade (16–18) can be deployed in the design of abiotic surfaces to minimize bacterial adhesion. Bacterial adhesion to engineered patchy soft surfaces has been studied before (19), but the possibility of patchiness on the bacteria themselves has not been considered in much detail.

We studied *E. coli* strain AB1157. Like all K-12 derivatives, it has mutations in the *rfb* gene cluster [here, in *rfbD* (20)] preventing O-antigen production (21). Thus, one major cause of variability and molecular roughness on the cell surface is absent. Our cells display a highly conserved layer of core oligosaccharides anchored to the outer membrane by lipid A (22), although the precise terminal sugars in AB1157 are unknown. Besides the wild-type (WT), to further simplify the surface, we also used a mutant (AD19 = AB1157 *fimA*[−], *fliF*[−]; hereafter ΔFF) defective in producing type 1 fimbriae and flagella. In transmission electron micrographs (fig. S1), these cells appear smooth down to $\lesssim 10$ nm. Any heterogeneities, or “patchiness,” on the surface of this mutant are likely due to membrane proteins.

RESULTS

A high-throughput method reveals complex adhesion behavior

To monitor surface adhesion of *E. coli*, we loaded cell suspensions into 400- μm -high borosilicate glass capillaries at $\sim 4.5 \times 10^7$ cells/ml (WT) or $\sim 1.5 \times 10^7$ cells/ml (ΔFF) in phosphate motility buffer (MB) and observed them in an inverted microscope at ca. 22°C using a 60 \times phase-contrast objective (focal depth ~ 3.5 μm) (Fig. 1A). From measurements at the lower surface at the start of the experiment, we estimate an initial motile fraction between 25 and 35% [nonadhering motile cells swim at an average speed of $\lesssim 20$ $\mu\text{m s}^{-1}$ (23)]; the remaining cells are nonmotile and diffuse as passive colloids. With 0.72 μM glucose included in the MB, the swimmers maintain their speed for at least 20 hours (23). Atomic force microscopy (AFM) measurements reveal that the glass surface is smooth, with a root-mean-squared roughness of 0.25 ± 0.003 nm (fig. S2).

Time-lapse images of the bottom and top glass surfaces were taken automatically at multiple locations to track arriving cells and their subsequent fate. We adapted algorithms used for colloidal rods (24)

Copyright © 2018
The Authors, some
rights reserved;
exclusive licensee
American Association
for the Advancement
of Science. No claim to
original U.S. Government
Works. Distributed
under a Creative
Commons Attribution
NonCommercial
License 4.0 (CC BY-NC).

¹Scottish Universities Physics Alliances and School of Physics and Astronomy, University of Edinburgh, James Clerk Maxwell Building, Peter Guthrie Tait Road, Edinburgh EH9 3FD, UK. ²Department of Physics, Soft Condensed Matter Debye Institute for Nanomaterials Science, Utrecht University, Princetonplein 5, 3584 CC Utrecht, Netherlands. ³School of Engineering, Institute for Materials and Processes, University of Edinburgh, Sanderson Building, Robert Stevenson Road, The King's Buildings, Edinburgh EH9 3FB, UK.
*Corresponding author. Email: t.vissers@ed.ac.uk

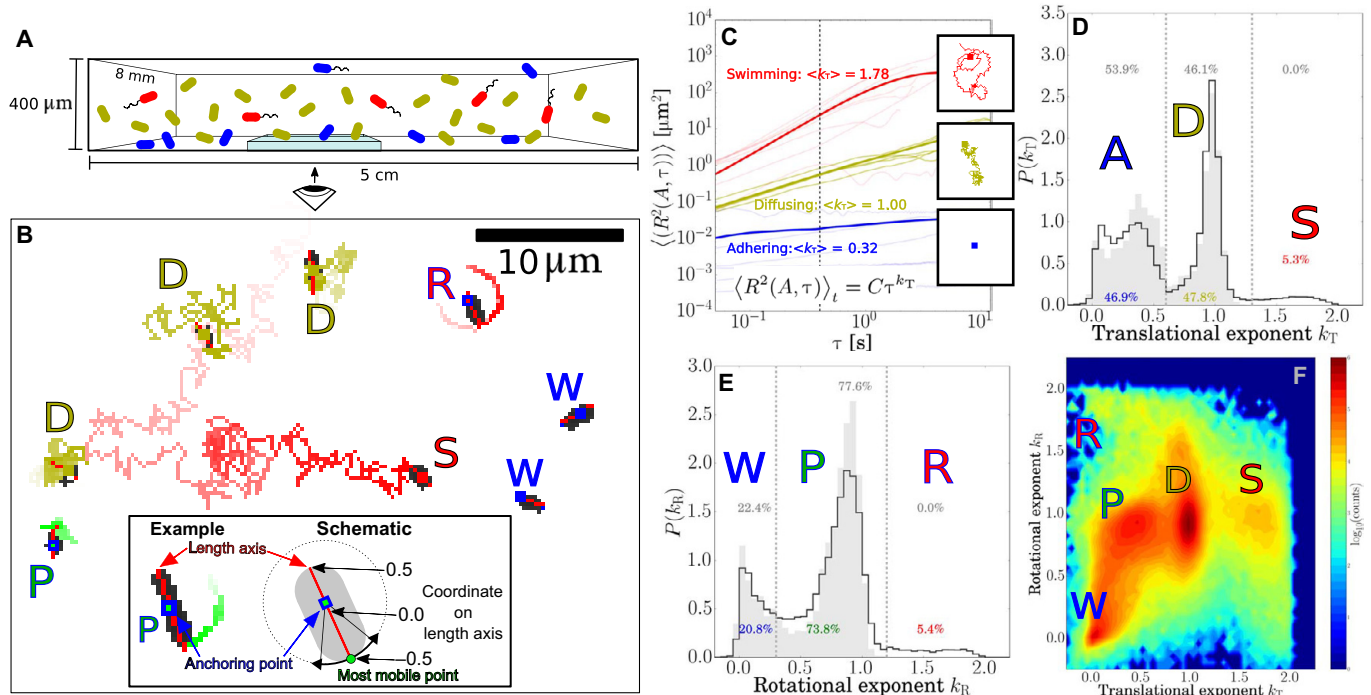


Fig. 1. Tracking and classification of bacteria. (A) Schematic of adhering (blue), diffusing (olive), and swimming (red) bacteria in a capillary. (B) Trajectories tracing the most mobile point on a cell. Straight red lines are fits of the length axis, squares mark anchoring points, and letters mark the type: diffuser (D), swimmer (S), wobbler (W), pivoter (P), and active rotator (R). The image is black/white-inverted and thresholded to be clear in print. Inset: Adhering cell and schematic depicting the anchoring coordinate and most mobile coordinate $\in [-0.5, 0.5]$ on its length axis. (C) MSDs as a function of time interval τ from trajectories of swimming (red), diffusing (olive), and adhering (blue) bacteria; thin lines show randomly selected individual trajectories and thick lines represent the average $\langle R^2(A, \tau) \rangle_t = C_T \tau^{k_T}$. The insets show an example trajectory for each category; squares denote the position in the last frame. (D) Normalized distribution of the translational exponent k_T for WT cells on glass during the first 2 hours of the experiment, showing distinct peaks for adhering (A), diffusing (D), and swimming (S) subpopulations. (E) Normalized distribution of the rotational exponent k_R for adhering cells, showing three peaks for wobblers (W), pivoters (P), and active rotators (R). Data in panels D and E for the nonflagellated mutant ΔFF are shown in gray. (F) Two-dimensional histogram (logarithmic scaling) of the translational (k_T) and rotational (k_R) exponents for WT cells, showing three peaks for adherers (W, P, and R), one for diffusers (D), and one for swimmers (S). The distributions in panels D to F are based on 139,335 cells for WT and 10,582 cells for ΔFF , and data are weighted for trajectory durations.

to determine the position \mathbf{r} , orientation θ , and projected length l_p of each cell (movie S1) and track these in time. Typical analyzed trajectories are shown in Fig. 1B and movie S2. Quantifying these trajectories allows us to classify cells' adhesive phenotypes.

Focusing first on translation, we identified for each cell the point of least motion along its length axis (fig. S3), corresponding roughly to the center of attachment for adhered cells and to the hydrodynamic center for free cells, and determined its mean-squared displacement (MSD) = $\langle (\mathbf{r}(t + \tau) - \mathbf{r}(t))^2 \rangle$. At short delay time ($\tau \leq 0.4$ s), all cells show MSD $\cong C_T \tau^{k_T}$, with a range of $\{C_T, k_T\}$ (Fig. 1C), exhibiting constrained, diffusive, or ballistic (directed) motion with values peaked around $k_T = 0, 1, \text{ or } 2$, respectively (25, 26).

The probability distribution of k_T , $P(k_T)$, shows three well-separated peaks (Fig. 1D), classifying cells into adherers (A), diffusers (D), or swimmers (S). Cells with $k_T \lesssim 0.6$ and $k_T \gtrsim 1.3$ correspond to adherers and swimmers, respectively. Diffusers show $0.6 \lesssim k_T \lesssim 1.3$; the spread and skewness of the distribution in this range come from the finite, stochastic trajectories used in tracking.

The initial analysis misidentified some diffusers as adherers and vice versa, for example, because of the width of the distributions and a few adherers that pivot around their poles and swing out of plane, showing up as rapid short-time motion. To resolve this issue, we further required that adherers be visible for at least 6 s. Trajectories with $k_T \lesssim 0.6$ and

shorter than 6 s were labeled as ambiguous. For trajectories greater than 6 s, we also calculated the translational exponents for the longer delay time of $\tau = 4$ s; we then used this exponent, k_T^{4s} , as a cell's translational exponent if both $k_T^{4s} < 0.6$ and $k_T^{4s} < k_T^{0.4s}$ and identified the trajectory on this basis.

Visual inspection of trajectories (movies S3 to S7) revealed correct automated classification of $\geq 95\%$ of all cells using this algorithm. The shallow minimum in $P(k_T)$ demarcating the D and S subpopulations coincides with the cutoff in $P(k_T)$ measured for the ΔFF mutant (Fig. 1E, gray), which does not swim.

Similarly, we fitted the mean-squared orientational displacement (MSOD) = $\langle (\theta(t + \tau) - \theta(t))^2 \rangle = C_R \tau^{k_R}$ for $\tau < 0.4$ s. The probability distribution of k_R , $P(k_R)$, for WT adherers shows two peaks falling off to a long "tail" at $k_R \sim 2$ (Fig. 1E). We interpret $k_R \sim 0$ as corresponding to adhering cells that "wobble" (W) around a fixed orientation; $k_R \sim 1$ as corresponding to cells that "pivot" (P) around a fixed attachment point and undergo apparently free rotational diffusion; and $k_R \sim 2$ as corresponding to cells that "rotate ballistically" (R).

Only adherers show three rotational modes. Diffusing and swimming cells both appear only as a single mode in k_R . This pattern is clear in the two-dimensional heat map of $\{k_T, k_R\}$ (Fig. 1F), which shows three features for adherers (W, P, and R), one for diffusers (D), and one for swimmers (S). Of the three different adhering modes, the active rotators

observed for WT strains were not found in ΔFF cells, which is reflected by the missing tail at $k_R > 1.3$ for ΔFF (gray area in Fig. 1E). We attribute ballistic rotation to the presence of active flagella (27), which we further verified using a strain modified to permit flagella staining (movie S8) (28). We observed that most rotating cells were found adhering with a point on or close to the body. From the movies, it appears that active rotation originated from direct adhesion by a rotating motor or short filament or, indirectly, by freely moving flagella rotating an otherwise adhering cell. We also observed cells “tethered” by a flagellum with the cell body not attached to the surface, but these occurrences were rare. Flagella-mediated adhesion is implicated in biofilm formation and pathogenicity (29, 30). It may be electrostatically mediated (31–33), so that its rarity ($\leq 6\%$ of cells; cf. Fig. 1E) under our high-ionicity conditions (Debye screening length $\kappa_D^{-1} \approx 1$ nm) is perhaps unsurprising. Hereafter, we mostly neglect active rotators and focus on wobblers and pivoters.

The pivoting state is particularly intriguing: The diffusive angular motion implies that the cell is attached at a single, freely rotating locus. We observed many cells pivoting more than 2π within a single movie. Virtually no pivoters were observed in the adhesion of sterically stabilized synthetic bacterium-shaped hollow silica particles (fig. S1) (34), so that such free rotation is not a generic feature of colloidal rods attached to surfaces. Neither is it due to surface organelles, because pivoters were well represented in WT and ΔFF strains and in further mutants ΔFH and ΔFFH , which additionally lacked the hook protein (fig. S4). We later examine this pivoting behavior in more detail.

In sum, tracking the translational and rotational motion of *E. coli* at a borosilicate glass surface has revealed a variety of adhesive behavior: Some cells adhere, others do not; of the adherers, a small number rotate ballistically, whereas most either wobble or undergo pivoted rota-

tional diffusion. The question naturally arises: Is this variety due to cells switching between different modes of behavior within our observational time scale or due to the presence of different kinds of cells? In statistical physics terms, is the “disorder” (presence of multiple modes of behavior) annealed or quenched? To answer this question, we turn our attention to the adhesion dynamics.

Adhesive propensity is phenotypically heterogeneous

We followed the arrival of cells on the lower capillary surface from the bulk (shown schematically in Fig. 2A) and observed the buildup of the different subpopulations to a steady state (Fig. 2B). The time between sealing the capillary and beginning observations ($\lesssim 10$ min) was long enough for the near-surface swimmers to achieve dynamic equilibrium with the bulk (35), so that we observed a roughly constant number of near-surface swimmers. Meanwhile, the number of adherers and diffusers both increased steadily before saturating after ~ 2 hours, which is consistent with nonswimmers sedimenting through the $h = 400$ μm capillary at an independently measured speed of $v_s = 0.06 \pm 0.01$ $\mu\text{m s}^{-1}$. There was no detectable delay between the arrival of the first diffusers and the first adherers (Fig. 2B), so that adhesion is rapid on the scale of 5 min. Repeating with ΔFF mutants gave qualitatively similar dynamics except for the absence of swimmers and rotators (Fig. 2C). From this, we infer that flagella and fimbriae are not essential to the observed WT phenomenology.

Figure 2B shows that more than half of the population does not adhere to the surface and that this fraction stays approximately constant over 14 hours. We will argue that this is primarily due to inherent, phenotypic heterogeneity between the cells. However, we must first exclude the alternative possibility that the incomplete adhesion is maintained by a dynamic equilibrium between surface binding and

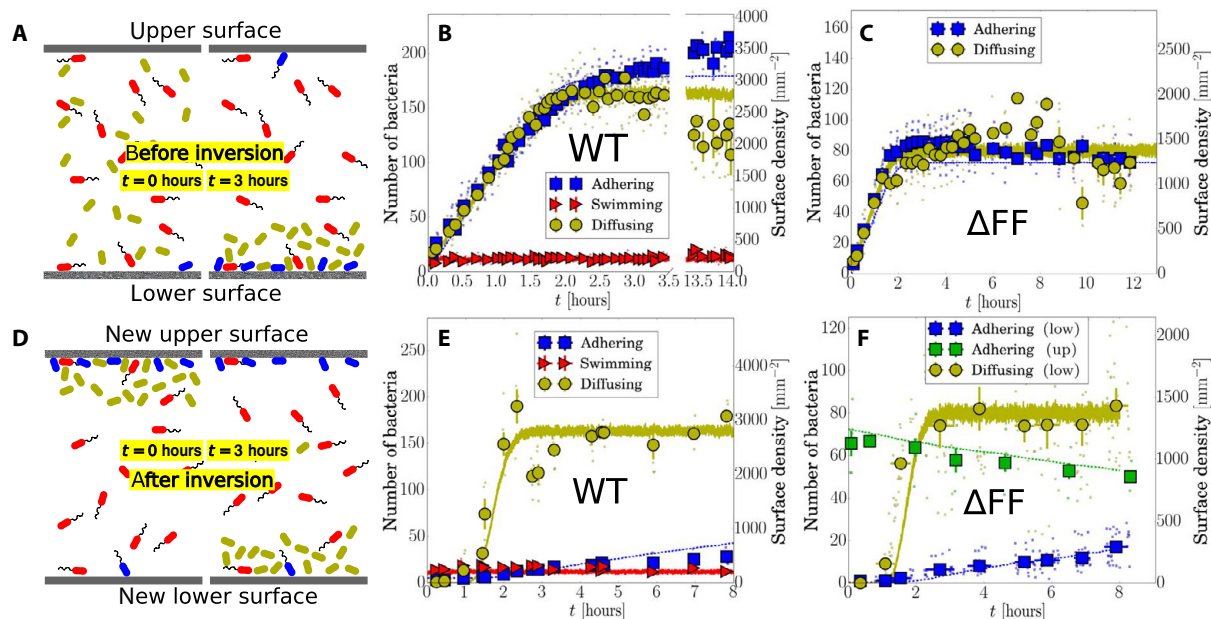


Fig. 2. Capillary inversion assay. (A) Schematic of adhering (blue), diffusing (olive), and swimming (red) cells in the capillary at loading (0 hours) and 3 hours after, when nonmotile cells have sedimented, and motile cells have reached the top and bottom surfaces. (B) Number of adherers, diffusers, and swimmers on the lower surface as a function of time for WT and (C) for ΔFF . (D) Schematic immediately (0 hours) and 3 hours after capillary inversion. (E) Number of cells on the lower surface after inversion for WT and (F) for ΔFF , where the number of adhering cells on the upper surface is also given. Small points are average values for single movies, and large points are weighted averages over groups of multiple movies, with vertical bars as the SE and horizontal bars as the time window for each point. The lines in panels B, C, E, and F are results from simulations with a minimal kinetic model.

unbinding of otherwise identical cells. For this, we use an inversion assay (36), in which we inverted the capillary and observed that nonadhering diffusing cells sediment toward the new lower surface, which, at this point, is virtually empty (Fig. 2D, left panel). When the sedimenting cells reach the new lower surface around 1 to 2 hours after inversion (Fig. 2, E and F), almost none of them adhere. This is inconsistent with a dynamic equilibrium between otherwise identical cells, for which we would expect the same ratio of diffusers to adherers on the lower surface before and after inversion. Therefore, we reason that there are differences between the adhesive properties of individual cells. In statistical physics terms, the disorder in adhesive propensity is quenched. This inversion assay also rules out a third possibility, that the number of adherers is limited by the availability of binding sites on the glass surface. In this unobserved scenario, we would expect phenotypically sticky cells, which were unable to find a binding site before inversion, to adhere post-inversion to the new, empty lower surface.

Over longer time scales, there is a slight increase in the number of adhering cells on the new lower surface for both ΔFF and WT cells. This increase is due to previously adhering cells detaching slowly from the new upper surface and sedimenting downward and reattaching to the new lower surface. We can show this by monitoring the decay in adherer numbers remaining on the (new) upper surface (green squares in Fig. 2F). Fitting the adherer number N to $N(t) = N(0)e^{-\gamma t}$ returns a detachment rate of $\gamma \approx 0.032 \text{ hour}^{-1}$. After the time it takes for detached adherers to sediment through the capillary (less than 2 hours), all of these cells appear at and re-adhere to the (new) lower surface, with the rate of this attachment being approximately equal to the detachment rate, as one would expect from our picture. This shows that the adhesion properties of individual cells are preserved in time: Cells that were previously adhering on the (new) upper surface, detach, and sediment downward are capable of reattaching on the (new) lower surface.

Postadhesion dynamics are also phenotypically heterogeneous

We next focus on adhering cells and distinguish between wobblers and pivoters on the basis of their MSOD. We report data for ΔFF mutants, for which there are no active rotators. As cells arrived on the lower capillary surface, the number of wobblers and pivoters increased linearly before saturating, showing a constant P/W ratio of 3:1 throughout (Fig. 3A). After capillary inversion, the dynamics of these two subpopulations diverged: Pivoters left the (new) upper surface at least an order of magnitude faster than wobblers, whose number remained almost constant (Fig. 3B). Thus, wobblers appear more tightly bound.

The rate of arrival of pivoters on the (new) lower surface (Fig. 3C) equaled the rate of their disappearance from the (new) upper surface (Fig. 3B), with a delay in arrival consistent with sedimenting through $400 \mu\text{m}$. The buildup of wobblers on the (new) lower surface commenced ≥ 1 hour after the arrival of the first pivoters, suggesting that pivoters may become wobblers. To confirm this, we monitored adherers on the lower surface before inversion over 8 hours in the steady state and measured the fraction of time F_w each cell spent as a wobbler (Fig. 3D): $\sim 70\%$ of cells were always pivoting, whereas the remainder switched between wobbling and pivoting.

The data in Fig. 3D are not consistent with a single population of adherers stochastically switching between wobbling and pivoting states, for which we expect a broad distribution peaked around some intermediate F_w . The sharp peak at $F_w = 0$ (always pivoting) implies at least two populations: a stochastically switching fraction and a pure pivoting fraction.

The interstate switching dynamics can be quantified (Fig. 3E) by a time-dependent transition matrix, $P_{ab}(\Delta t)$, giving the probability of a cell in state “a” at time t being in state “b” at time $t + \Delta t$, where $\{a\} = \{P, W\}$ and $\{b\} = \{P, W, O\}$, with P, W, and O standing for pivoting, wobbling, and off, respectively, with the latter denoting a cell detaching

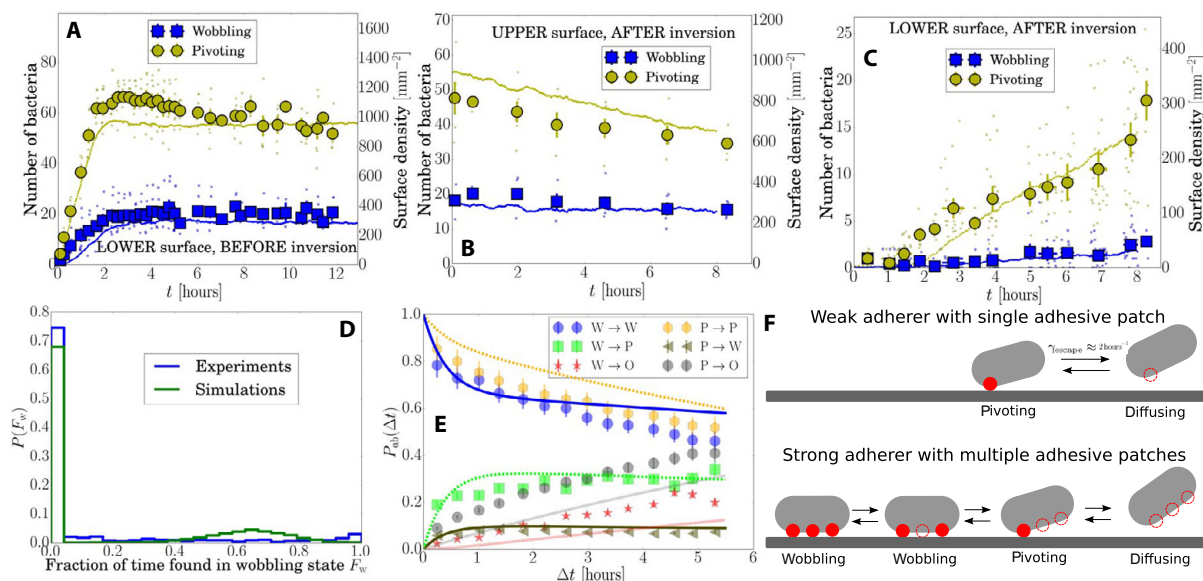


Fig. 3. Polydispersity in adhering cells for ΔFF . (A) Number of wobbling and pivoting cells on the lower surface before capillary inversion and (B and C) on the upper and lower surface after capillary inversion. Solid lines in panels A to C are from simulations with a minimal kinetic model. Data correspond to the inversion experiments in Fig. 2 (C and F). (D) Histogram showing the fraction of time cells are identified as wobbling on the lower surface before inversion, as in experiments (from a total of 117 movies over six different positions recorded between 4 and 12 hours before capillary inversion) and simulations. (E) Probabilities for a cell in a wobbling (W) or pivoting (P) state at time t to be found wobbling, pivoting, or off the surface (O) at a later time $t + \Delta t$ (lines are for the kinetic model). (F) Schematic of weakly and strongly adhering cells: filled red circle, bound adhesive patch; empty circles, unbound adhesive patch.

from the surface altogether. There is significant $P \leftrightarrow W$ switching on a time scale of several hours. However, some cells are mostly in either the P state or the W state: Only $\sim 10\%$ of originally P cells become W cells and $\sim 30\%$ of originally W cells become P cells. The discernible rate of $W \rightarrow O$ transitions explains the slow buildup of wobblers on the (new) lower surface after inversion (Fig. 3C). Direct visual analysis of the trajectories confirms that $W \rightarrow O$ transitions occurred via the sequence $W \leftrightarrow P \rightarrow O$. This implies that wobbling cells detaching from the upper surface first become pivoters before they detach and that they reattach as pivoters before becoming wobblers. On the lower surface before inversion, detachments and reattachments of cells occurred at a steady rate over time scales of hours. Detached cells were rarely observed to reattach at the same site but almost always at alternative locations on the surface (fig. S5 and movie S9), which again demonstrates that adhesion is not limited by a low number of binding sites on the glass substrate.

In sum, we conclude that adhering cells are also phenotypically heterogeneous and can either be purely pivoting or switch between pivoting and wobbling states. Moreover, a pivoting cell may relatively easily detach from the surface, whereas wobbling cells can only do so by first becoming pivoters.

A patchy-colloid model explains *E. coli* adhesion dynamics

In a simple model consistent with our observations (Fig. 3), cells may have 0, 1, or ≥ 2 adhesive patches available for simultaneous surface binding. Cells without patches are permanent nonadherers. Cells with 1 patch are “pure pivoters”—such a cell bound to a surface using its single adhesive patch may detach stochastically because of thermal motion. Cells with ≥ 2 patches may be actually bound to a surface at ≥ 2 , 1, or 0 of these patches and appear as a wobbler, pivoter, or a free diffuser. Note that our ΔFF mutant data show that these patches are not necessarily (if at all) associated with flagella or fimbriae. Moreover, in our model, cells with at least one available adhesive patch will eventually encounter the surface with this patch because of rotational diffusion. This mimics reality, where the rotational self-diffusion time in bulk $\tau_{\text{self,rot}} \approx (2\pi)^2/4D_{\text{rot}} \approx 1$ min for a free cell [using typical measured values for D_{rot} for deflagellated *E. coli* (37)], so that it can explore many different orientations during an experiment.

The observed rate at which pivoters leave the upper capillary surface after inversion ($\gamma \approx 0.032 \text{ hour}^{-1}$; Fig. 3B) allows us to estimate the adhesive strength of a single patch. A particle confined to a potential of depth ΔU escapes at rate (38)

$$\gamma = \left(\frac{\kappa_S D}{2\pi k_B T} \right) \exp\left(-\frac{\Delta U}{k_B T}\right) \quad (1)$$

Here, k_B is Boltzmann’s constant, T is the temperature, and D is the particle’s diffusivity inside a potential well of stiffness κ_S . Dimensional analysis suggests that $\kappa_S \approx \Delta U/L^2$, where L is the interaction range. From AFM, we estimate $20 \lesssim L \lesssim 100$ nm for bacteria adhering to a variety of surfaces (39, 40). Separately, from the typical maximum MSD of the anchoring coordinate of pivoting cells, we estimate $L \lesssim 200$ nm (fig. S6). ΔU is rather insensitive to the exact value used. Taking a conservatively broad range of $5 \text{ nm} < L < 150 \text{ nm}$ and $D = 0.4 \mu\text{m}^2 \text{ s}^{-1}$ (41), we obtain $15 k_B T < \Delta U < 23 k_B T$. This is well within the range of, for example, electrostatic and hydration effects (42) and hydrophobic interactions (43) between glass and proteins (44) or lipopolysaccharides (45). We note that if electrostatic attractions were to play a role

in adhesion, these are likely very local because of the smallness of the Debye screening length ($\kappa_D^{-1} \approx 1$ nm) and the fact that the bacterial surface bears a net negative charge (zeta potential = -16 mV measured for our WT strain). The latter observation means that any electrostatic attraction with a negative glass surface (33) must be due to localized minority positive charges on the bacterium arising from, for example, amine and hydroxyl groups at around neutral pH (9).

In a previous work where an inversion assay was used (36), it was suggested that gravitational pull might contribute to the detachment of cells from the upper surface (after inversion). The potential energy difference due to gravity for displacing a cell over a distance comparable to the interaction range, $U_g \approx 0.05 k_B T$, is much smaller than our estimated binding energy of an adhesive patch and therefore has a negligible effect on the detachment rate. Nonetheless, gravity causes a more subtle difference between the adhesion dynamics on the lower and upper surfaces. Once a cell on the upper surface detaches, it immediately starts sedimenting downward (away from the surface), making it highly improbable that it will reattach. On the lower surface, detaching cells remain close to the same surface and reattach to it eventually.

To deduce the likely maximum number of adhesive patches on our cells available for simultaneous surface binding, we consider the statistics of the point of minimum translation (“anchoring point,” $-0.5 \leq A \leq 0.5$; Fig. 1B, inset). The distribution of anchoring points for wobblers (≥ 2 patches) is given by some weighted average over the individual patch locations (see the Supplementary Materials) and so must be narrower than that for a pivoter with a single patch. Figure 4 plots the observed normalized distribution of the anchoring coordinate $|A|$ for pivoters (Fig. 4A) and wobblers (Fig. 4B), being narrower for the latter (SDs 0.27 and 0.22, respectively). We modeled the anchor-point distribution for adherers with n patches (Fig. 4B), assuming that these patches are placed along the cell axis according to the $P(|A|)$ for pivoters, and that the anchoring coordinate for a wobbler is the average of the coordinates for these patches (see the Supplementary Materials). Our data suggest $n = 2$ or 3. This is as expected: Higher n would mean that pivoters and nonadherers should be very rare and that wobblers would almost never detach, contrary to observations.

Note that the experimental distribution of $|A|$ for pivoters is slightly peaked near the cell center ($|A| \approx 0$) and toward the cell pole ($|A| \approx 0.3$) (Fig. 4A). The former is an artifact: A spherocylindrical cell adhering at one pole will appear as a small circle with an adhesion point identified in the cell center, artificially shifting the distribution toward $|A| = 0$. This can be removed by excluding cells with small projected lengths (orange line), although this does not significantly modify the predicted $P(|A|)$ for wobblers. The other peak indicates that cells have a slight preference for polar adhesion, as previously found for other strains (36, 46). The observation that the peak is not at the pole itself is again due to the cell’s spherocylindrical shape.

We can simulate a minimal kinetic model based on the schematic in Fig. 3F. Bacteria are modeled as noninteracting point particles in a box with periodic boundary conditions in the horizontal (x, y) plane and impenetrable boundaries in the vertical (z) direction. Cells diffuse and sediment toward the lower surface. For ΔFF mutants, there are three independent subpopulations: nonadherers that do not bind to the surface; weak adherers that bind to the surface to become pivoters at rate k_{adh} when within a distance Δz_{adh} ; and strong adherers that bind to the surface as pivoters, also at k_{adh} , and can switch stochastically to a wobbling state or back, respectively, with rates k_{PW} and k_{WP} . Both weak and strong adherers can only detach from the surface, at rate k_{det} when in the pivoting state.

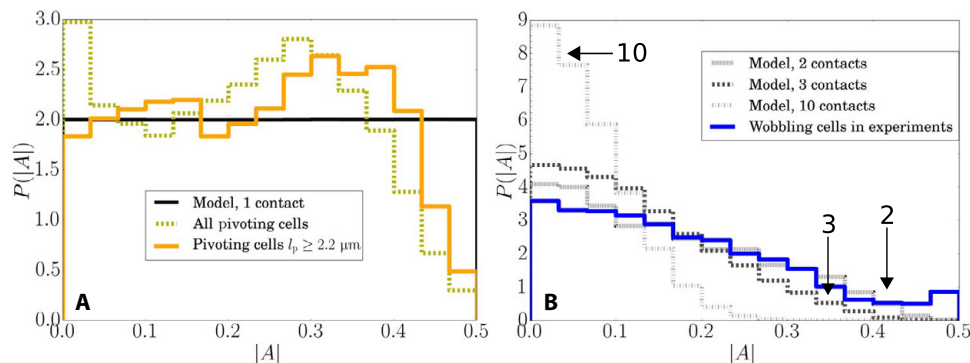


Fig. 4. Distributions of anchoring coordinates for ΔFF . (A) The measured distribution of anchoring coordinates $|A|$ for all pivoting cells (olive, 11,359 cells), only pivoting cells with $l_p > 2.2 \mu\text{m}$ (orange, 4338 cells) and for modeled cells with one contact point (black line). (B) The measured distribution of wobbling cells (blue, 4099 cells) fits best with models of cells with two or three patches. Modeled distribution of cells with 10 patches is also shown and peaks sharply close to zero. Modeled wobbler distributions were calculated using the $P(|A|)$ for pivoters with artifacts removed.

The model uses values of the diffusivity and sedimentation speed based on independent measurements, and $\Delta z_{\text{adh}} = 100 \text{ nm}$, in line with the typical interaction range. Fitting the on-surface switching dynamics (Fig. 3E) gives estimates for k_{PW} , k_{WP} , and the ratio of weak to strong adherers. Varying the remaining parameters, k_{adh} , k_{det} , and the total numbers of adherers and nonadherers credibly reproduces the main features of all our observations (curves in relevant parts of Figs. 2 and 3). We model the WT cells in the same way, except that a fraction of cells can swim and a subfraction of those can adhere as active rotators. The cell numbers are fitted, but the swimming speed is measured independently. Full model details are given in the Supplementary Materials, including used cell numbers (table S1) and movies depicting the simulations (movies S10 and S11).

DISCUSSION

We investigated the adhesion of *E. coli* AB1157 in buffer solution to glass. Using high-throughput and big-data analysis methods, we found strong heterogeneities between individual cells within a clonal population that are not related to type 1 fimbriae or flagella. These heterogeneities appear in the propensity for adhesion as well as the postadhesion dynamics. At least two types of adherers exist. Freely pivoted weak adherers are rotationally unconstrained and detach relatively easily. Strong adherers switch between this pivoting state and a rotationally constrained wobbling motion, in which they are more firmly bound to the surface.

A model of cells with adhesive patches that bind and unbind stochastically to the surfaces can explain our results. In this model, what differentiates subpopulations is the number of accessible patches per cell. Nonadhering cells have no patches and are always freely diffusing, weak adherers have one patch, and strong adherers have multiple adhesive patches that can bind simultaneously. These patches are estimated to have an interaction range of $\lesssim 100 \text{ nm}$ and contact energy of 15 to $23 k_{\text{B}}T$. A very recent direct measurement of two Gram-positive species of *Staphylococcus* bacteria (47) shows that their adhesion to surfaces is mediated by sticky patches of radii ~ 100 to 300 nm , from which an interaction range of $20 \lesssim L \lesssim 120 \text{ nm}$ is obtained. Thus, the physical mechanisms we have deduced from our experiments for *E. coli* may well be generic, even where specific details vary, for example, the interaction strengths measured in (47) are much larger, at $>10^3 k_{\text{B}}T$.

However, the properties of the bacterial surface depend on many variables. Thus, for example, the acid-base properties of the surfaces of *E. coli* K-12 and *Bacillus brevis* cells are dependent on species, growth phase, as well as the composition of the growth media (48). These properties also change upon adhesion (9). When initial adhesion leads to the formation of a full-blown biofilm, different adhesive proteins are involved in binding cells to the substrate or to each other (10, 49). Both population variations in adhesion strength (50) and the location on the cell surface of adhesive interactions (51) are of importance. The study of a variety of organisms under diverse conditions will therefore be needed to establish a full picture.

Our work raises important questions about the biomolecular details of adhesion, most obviously the nature of the adhesive patches. Their rotational freedom implicates membrane proteins, which can rotate freely in lipid bilayers (52), whereas the interaction range of $L \sim 100 \text{ nm}$ suggests the involvement of cell surface macromolecules, consistent with a recent suggestion based on more direct, AFM measurements (47). Such rotational freedom raises the further question of the possible translational freedom of these patches, because individual proteins can also translate diffusively in the bacterial outer membrane (53). Both motions are strongly dependent on temperature because of lipidic phase transitions. If future work finds these adhesive patches to have temperature-dependent mobility, then bacteria will constitute a new class of patchy colloids. The interaction of mobile adhesive patches with rough (54) and patchy (19) substrates offers intriguing possibilities.

Another key question is the origin of the phenotypic heterogeneity we observed. This may be an instance of phase variation—the reversible switching on and off of gene expression (55), often of surface structures (56). On the other hand, adhesion may trigger a process of diversification in gene expression analogous to the process discovered recently in biofilm formation (57). Elucidating these issues using modern tools for time-dependent gene and protein expression assays is now an urgent task.

Finally, our work has implications for the design of antiadhesion surfaces, which is a key part of the ongoing fight against bacterial infections. First, it appears that we must now think in terms of designing antiadhesion surfaces that account for the range of adhesive phenotypes. Second, designing antiadhesion technologies will involve computer simulations, which, however, will never be fine-grained enough to include all details. Our finding that bacteria are patchy colloids vis-à-vis surface adhesion can help to design viable coarse-graining strategies and

59. M. S. Guyer, R. R. Reed, J. A. Steitz, K. B. Low, Identification of a sex-factor-affinity site in *E. coli* as $\gamma\delta$, in *Cold Spring Harbor Symposia on Quantitative Biology* (Cold Spring Harbor Laboratory Press, 1981), vol. 45, pp. 135–140.
60. T. Baba *et al.*, *Mol. Syst. Biol.* **2**, 2006.0008 (2006).

Acknowledgments: We thank A. Jepson, A. Morozov, J. Thijssen, M. Cates, R. di Leonardo, F. Sciortino, A. Lips, T. Pilizota, A. Lepore, and H. Berg for useful discussions. **Funding:** T.V. was funded by FP7-PEOPLE-2013-IEF Marie Curie fellowships (LivPaC, 623364) and N.K. through H2020-MSCA-IF-2014 (ActiDoC, 654688). J.M.F. held an Engineering and Physical Sciences Research Council (EPSRC) studentship (EP/L015536/1 SOFI CDT), and A.T.B. received funding from a University of Edinburgh Chancellor's Fellowship. Others were funded by EPSRC program grant EP/J007404/1 and European Research Council Advanced Grant GA 340877-PHYSAPS. We acknowledge the support of the Wellcome Trust Multi-user Equipment Grant (WT104915MA) for recording the transmission electron microscopy (TEM) images. **Author contributions:** T.V. and W.C.K.P. designed the research. A.D. constructed the mutants. A.D. and J.S.-L. prepared the bacteria. A.B.S. prepared the silica-coated bacteria and performed the scanning electron microscopy measurements. T.V. performed the adhesion experiments. V.A.M. assisted in the preliminary experiments, microscopy setup, and measurement protocols. J.M.F. and V.K. performed the AFM measurements. J.M.F. and T.V. performed TEM measurements. T.V., A.T.B., N.K., M.H., and W.C.K.P. analyzed the data. A.T.B. and T.V. performed the modeling. V.A.M., J.A., and N.K. assisted with the experiments. T.V., A.T.B., and W.C.K.P. wrote the paper. All authors discussed the results and commented on the manuscript. **Competing interests:** The authors declare that they have no competing interests. **Data and materials availability:** Data used in this publication are available on the Edinburgh DataShare repository (DOI: <http://dx.doi.org/10.7488/ds/2315>). All other data needed to evaluate the conclusions in the paper are present in the paper and/or the

Supplementary Materials. Additional data related to this paper may be requested from the authors.

Submitted 29 June 2017

Accepted 7 March 2018

Published 27 April 2018

10.1126/sciadv.aao1170

Citation: T. Vissers, A. T. Brown, N. Koumakis, A. Dawson, M. Hermes, J. Schwarz-Linek, A. B. Schofield, J. M. French, V. Koutsos, J. Arlt, V. A. Martinez, W. C. K. Poon, Bacteria as living patchy colloids: Phenotypic heterogeneity in surface adhesion. *Sci. Adv.* **4**, eaao1170 (2018).

SUPPLEMENTARY MATERIALS

Supplementary material for this article is available at <http://advances.sciencemag.org/cgi/content/full/4/4/eaao1170/DC1>

section S1. Characterization

section S2. Synthesis and experimental details of bacterium-shaped hollow silica particles

section S3. Determining the anchoring point of a cell and classifying its dynamics

section S4. Adhesion for mutants without the flagellar hook

section S5. Pivoters, wobblers, and deserted adhesion sites

section S6. MSDs of anchoring point for wobblers and pivoters

section S7. Kinetic model details

fig. S1. Electron microscopy images of *E. coli* WT and Δ FF and bacterium-shaped hollow silica particles.

fig. S2. AFM images of the inner surface of the glass capillaries.

fig. S3. MSDs and anchoring points on the length axis of different types of bacteria.

SYNTHETIC BIOLOGY

Programming self-organizing multicellular structures with synthetic cell-cell signaling

Satoshi Toda¹, Lucas R. Blanch², Sindy K. Y. Tang²,
Leonardo Morsut^{1*†}, Wendell A. Lim^{1†}

A common theme in the self-organization of multicellular tissues is the use of cell-cell signaling networks to induce morphological changes. We used the modular synNotch juxtacrine signaling platform to engineer artificial genetic programs in which specific cell-cell contacts induced changes in cadherin cell adhesion. Despite their simplicity, these minimal intercellular programs were sufficient to yield assemblies with hallmarks of natural developmental systems: robust self-organization into multidomain structures, well-choreographed sequential assembly, cell type divergence, symmetry breaking, and the capacity for regeneration upon injury. The ability of these networks to drive complex structure formation illustrates the power of interlinking cell signaling with cell sorting: Signal-induced spatial reorganization alters the local signals received by each cell, resulting in iterative cycles of cell fate branching. These results provide insights into the evolution of multicellularity and demonstrate the potential to engineer customized self-organizing tissues or materials.

During the development of multicellular organisms, tissues self-organize into the complex architectures essential for proper function. Even with minimal external instructions, cells proliferate, diverge into distinct cell types, and spatially self-organize into complex structures and patterns. Such self-organized structures are radically different from most human-made structures, because they are not assembled from preexisting parts that are physically linked according to a defined Cartesian blueprint. Rather, these structures emerge through a series of genetically programmed sequential events. To test and better develop our understanding of the principles governing multicellular self-organization, it would be powerful to design synthetic genetic programs that could direct the formation of custom multicellular structures (1–7).

Extensive studies of natural developmental programs have implicated many genes that control cell-cell signaling and cell morphology. Despite their molecular diversity, a common theme in these developmental systems is the use of cell-cell signaling interactions to conditionally induce morphological responses (8, 9). Thus, we explored whether simple synthetic circuits in which morphological changes are

driven by cell-cell signaling interactions could suffice to generate self-organizing multicellular structures.

A simple toolkit for engineering morphological programs

As a modular platform for engineering new, orthogonal cell-cell signaling networks, we focused on using the synthetic notch (synNotch) receptor system (Fig. 1A). SynNotch receptors contain the core regulatory domain of the juxtacrine signaling receptor Notch, linked to a chimeric extracellular recognition domain (e.g., single-chain antibody) and a chimeric intracellular transcriptional domain (10). When it recognizes its cognate ligand on a neighboring cell, the synNotch receptor undergoes cleavage of the transmembrane region, releasing the intracellular transcriptional domain to enter the nucleus and drive the expression of user-specified target genes. Thus, we can design synthetic cell-cell communication programs using synNotch circuits. SynNotch receptor-ligand pairs do not cross-talk with native signaling pathways such as Notch-Delta, or with one another, as long as they have different recognition and transcriptional domains. Here, we used two synNotch receptor-ligand pairs—an anti-CD19 single-chain antibody (scFv) receptor paired with CD19 ligand, and an anti-green fluorescent protein (GFP) nanobody receptor paired with surface GFP ligand—as orthogonal cell-cell communication channels.

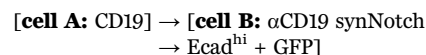
We created potential developmental programs by linking synNotch signaling to two possible transcriptional outputs: (i) expression of specific cadherin molecules (E-, N-, and P-cadherins), which lead to homotypic cell-cell adhesion and differential sorting of cells expressing different classes of adhesion molecules (11–13); and (ii) expression

of new synNotch ligands (Fig. 1A). Morphological sorting driven by cadherin expression can change what cells are next to each other, thus altering what synNotch signals will or will not be transmitted. Similarly, expression of new synNotch ligands can also create a subsequent stage of new cell-cell signals. Consequently, both of these outputs can propagate regulatory cascades by generating new signaling interactions between cells in the collective assembly.

We also constructed the synNotch circuits so that they drive expression of different fluorescent proteins, allowing color to indicate “differentiation” into new cell types (Fig. 1B). We expressed these synNotch circuits in mouse L929 fibroblasts, placed the cells in a low-adhesion U-bottom well (14), and followed their organization over time by fluorescence microscopy. L929 cells do not self-organize; normally, they only form a loose and randomly organized multicellular aggregate. We then tested whether any of the synthetic circuits we constructed from this small set of components could drive higher-order self-organization.

Engineering interacting cells that self-organize into a two-layer structure

We first focused on engineering two cell types that, when mixed, might communicate with and activate one another to induce the formation of a self-organized structure. We engineered a sender cell that expresses the synNotch ligand CD19 and blue fluorescent protein (BFP) (cell A) and a receiver cell that expresses the cognate anti-CD19 synNotch receptor and its response element (cell B). To induce cell sorting as an output of synNotch signaling, we placed the E-cadherin (Ecad) and GFP genes under the control of the synNotch-responsive promoter in the receiver cells (cell B in Fig. 2A). The circuit is represented by the following scheme:



As predicted, when cocultured with A-type sender cells, B-type receiver cells were activated to express Ecad and GFP (C-type cell phenotype). Subsequently, the green (GFP) C-type cells self-sorted to form a tight inner core, resulting in a well-defined two-layer structure (Fig. 2, B and C). Without induction of Ecad, the A- and B-type cells remained well-mixed (fig. S1A). When the synNotch signaling was inhibited by the γ -secretase inhibitor (2S)-N-[(3,5-difluorophenyl)acetyl]-L-alanyl-2-phenylglycine 1,1-dimethylethyl ester (DAPT), which blocks synNotch cleavage and signaling, sorting into two layers did not occur, as the inhibitor blocked the Ecad induction response in B-type cells (fig. S1B).

Using a bidirectional signaling cascade to engineer a self-organizing three-layer structure

To create more a complex structure, we added an additional layer of reciprocal cell-cell signaling to the above two-layer circuit (Fig. 2D). We engineered

Copyright © 2018
The Authors, some
rights reserved;
exclusive licensee
American Association
for the Advancement
of Science. No claim to
original U.S. Government
Works.

¹Department of Cellular and Molecular Pharmacology, Howard Hughes Medical Institute, and Center for Systems and Synthetic Biology, University of California, San Francisco, CA 94158, USA. ²Department of Mechanical Engineering, Stanford University, Stanford, CA 94305, USA.

*Present address: Eli and Edythe Broad CIRM Center for Regenerative Medicine and Stem Cell Research, University of Southern California, Los Angeles, CA 90033, USA.

†Corresponding author. Email: leonardo.morsut@med.usc.edu (L.M.); wendell.lim@ucsf.edu (W.A.L.)

the receiver (B-type) cell so that in addition to inducibly expressing Ecad, it also inducibly produced surface-tethered GFP as a synNotch ligand (GFP_{lig}). This modified form of GFP is constructed by fusion with the platelet-derived growth factor receptor transmembrane (PDGFR TM) domain (10). Surface-tethered GFP served as both a fluorescent reporter of the new cell type and a ligand for a secondary synNotch receptor with the cognate anti-GFP nanobody binding domain. In the sender cells, which constitutively express BFP and CD19 ligand, we also expressed the anti-GFP synNotch receptor, which when induced would drive expression of a low amount of E-cadherin (Ecad^{lo}) fused with an mCherry reporter for visualization. Thus, the interaction between this pair of cell types can in principle yield a two-step cascade of reciprocal signaling: In the first step, CD19 on cell A activates anti-CD19 synNotch in cell B to induce expression of a high level of E-cadherin (Ecad^{hi}) and the GFP_{lig}. In the second step, the GFP_{lig} on cell B can reciprocally activate the anti-GFP synNotch receptors in neighboring A-type cells to induce a low level of E-cadherin alongside the mCherry reporter. In this case, the A-type cell starts out as a sender cell but later becomes a receiver cell. The circuit is represented by the following scheme:

[cell A: CD19; αGFP synNotch]
 → [cell B: αCD19 synNotch → Ecad^{hi} + GFP_{lig}]
 → [cell A: αGFP synNotch → Ecad^{lo} + mCherry]

This circuit was predicted to form a three-layer structure: a green internal core (Ecad^{hi} + GFP) with the highest homotypic adhesion, an outer layer of blue cells (no Ecad), and a new population of red (Ecad^{lo} + mCherry) cells at a middle interface layer (Fig. 2E). We first engineered and established cell A and cell B lines from single-cell clones, and then confirmed that they showed synNotch-driven expression of high or low amounts of Ecad along with the appropriate marker fluorescent proteins (fig. S2A).

When we cocultured 200 A-type cells and 40 B-type cells, a three-layer structure was robustly formed, with a development process that required ~20 hours to fully unfold (Fig. 2F, fig. S2B, and movie S1). The structure emerged in a stereotypical stepwise fashion: induction of the green cells, sorting to form an inner core, and then the formation of a red middle layer. Here, the cascade of cell sorting and reciprocal signaling from the green core cells drives fate branching of the original A-type sender cells into two distinct fates (red and blue). Thus, this program has substantial ordering power: (i) The program generates an increased number of cell types (two cell genotypes become three phenotypic cell types), and (ii) the program leads to spatial sorting into three distinct compartments. This change represents a decrease in entropy relative to the starting point of a random mixture of two cell types, as shown in the cell lineage map (Fig. 2E). Many of these features of increased self-

ordering observed in this engineered assembly mimic the behavior of natural developmental systems, such as the simple formation of distinct progenitor cell types in early embryogenesis (15, 16).

The observed self-organization could be blocked by disrupting either synNotch signaling or cadherin expression. When we blocked cell-cell signaling with an inhibitor of synNotch signaling (DAPT), we observed no increase in cell types and no cell sorting into distinct layers (Fig. 2G and fig. S3B). When we removed E-cadherin expression from the system (fig. S3A), the assembled cells induced expression of the GFP and mCherry markers, but the different cell types remained randomly mixed

(Fig. 2G). Thus, the interlinking of signaling and cell sorting is required for cell fate divergence and spatial ordering.

Synthetic assembly is robust, reversible, and self-repairing

To see how reproducibly the synthetic cell-cell signaling program could drive three-layer formation, we followed 28 independent replicate cocultures starting with 200 A-type cells and 40 B-type cells (Fig. 3A). In most wells (57%), cells formed a single three-layer spheroid. In other wells, we observed “twin” multicore three-layer spheroids (21%) or multiple (separate) three-layer spheroids in the same well (11%).

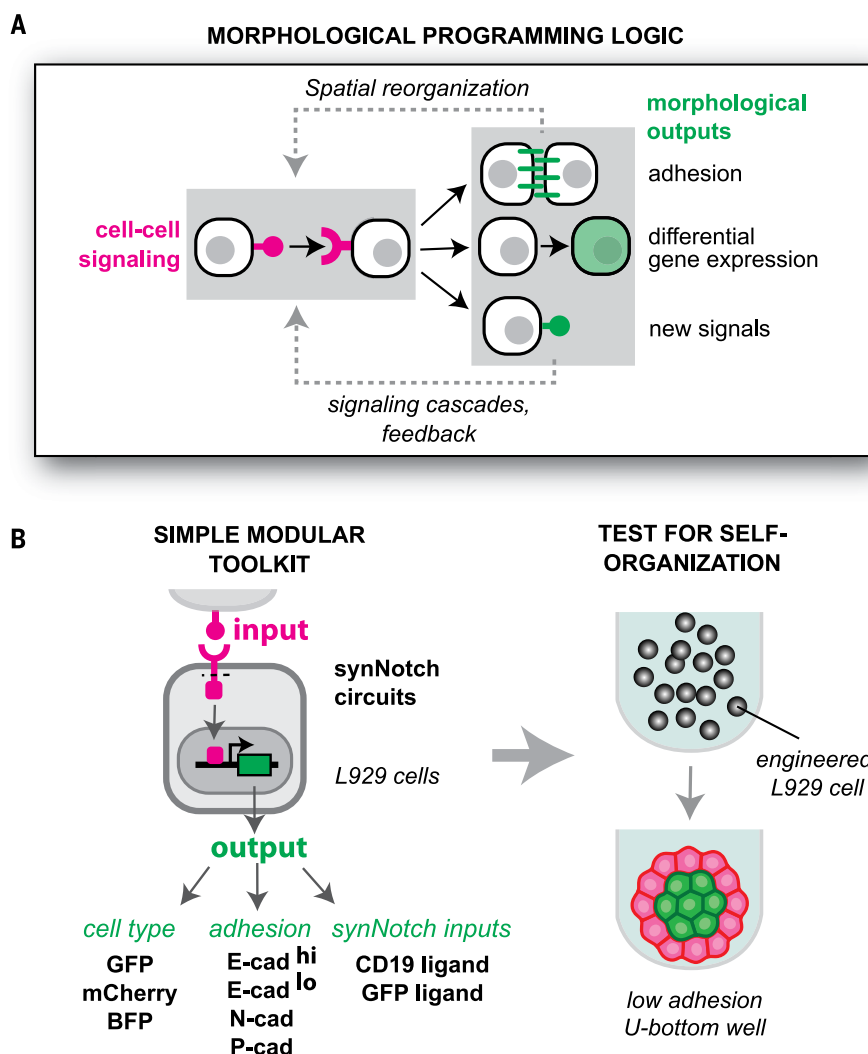


Fig. 1. Engineering cell-cell communication networks to program synthetic morphogenesis.

(A) Design logic underlying our synthetic morphogenesis circuits. Engineered cell-cell signaling is used to drive changes in cell adhesion, differentiation, and production of new cell-cell signals. These outputs can subsequently be propagated to generate new cell-cell signaling relationships. (B) Molecular components used for assembly of simple morphological circuits. We used two synNotch ligand-receptor pairs (surface ligands CD19 and GFP) for cell signaling, three fluorescent proteins as markers of “differentiation,” and several cadherin molecules (expressed at different levels) as morphological outputs. Engineered circuits are transduced into L929 fibroblast cells, placed in defined numbers in low-adhesion U-bottom wells, and screened by microscopy for spatial self-organization.

Thus, the overall three-layer architecture of green, red, and blue cells was robustly generated in ~90% of the cultures. A 3D reconstruction image of three-layer structure is shown in Fig. 3B and movie S1. Three-layer formation was robust to variation in the initial number or ratio of starting cells (fig. S2C). Only when we used a low number of starting A-type cells did we begin to see formation of two-layer structures (green and red only), because all the A-type cells were converted to Ecad^{lo} cells (i.e., the number of A cells was limiting).

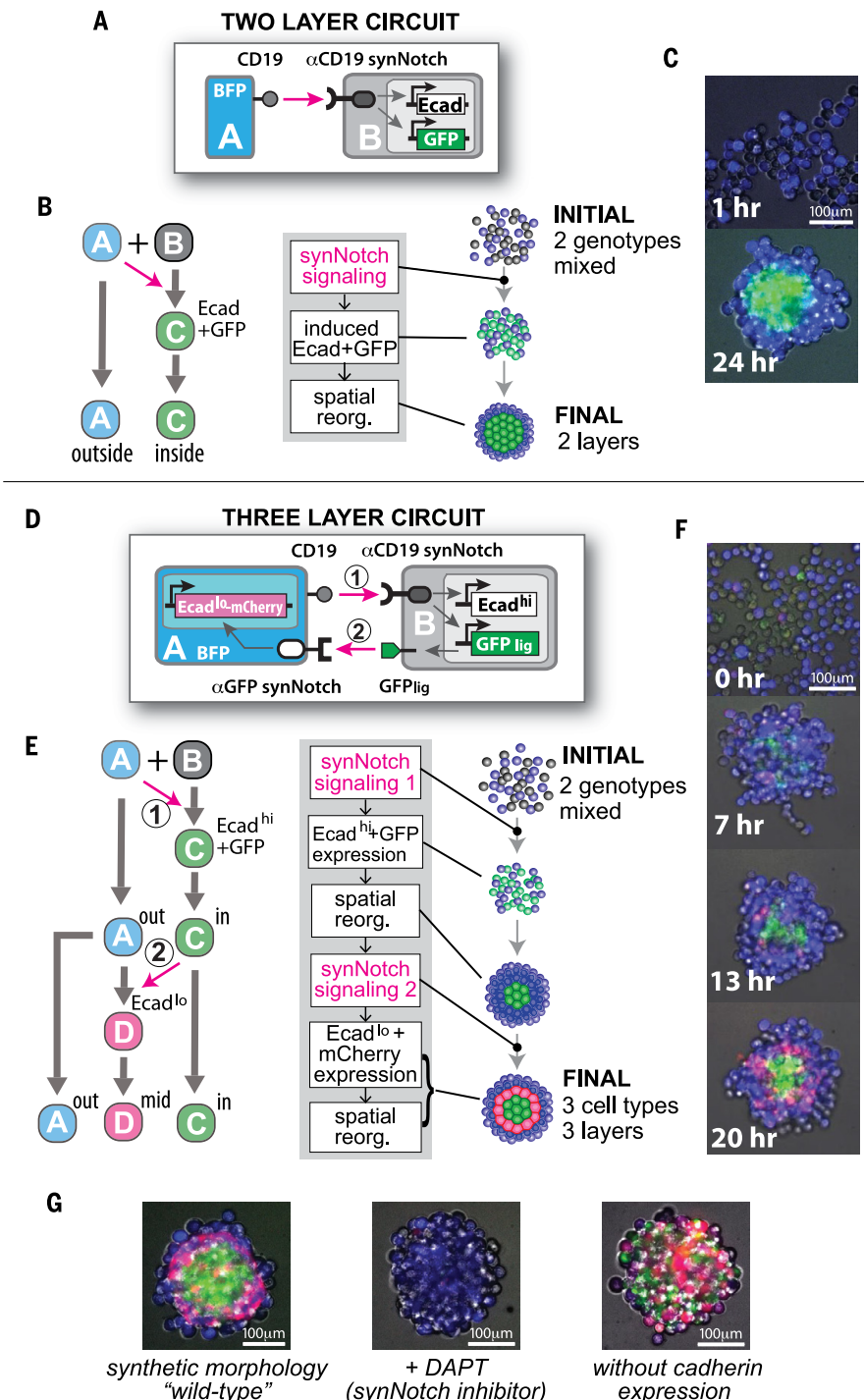
In many cases, natural self-organized tissues have an ability to regenerate after injury (17). To test how this three-layer structure would respond to injury, we cut the structure into two fragments with a microfluidic guillotine system (18) (movie S2). Immediately after cleavage, the GFP-positive core cells were exposed to the surface, but within 24 hours, the green core cells were re-enveloped by the red layer, regenerating the spherical three-layer structure (Fig. 3C). To further test the reversibility of the self-assembled three-layer structure, we added the synNotch inhibitor DAPT to pre-

formed structures. The layered structure and distinct cell types were totally disrupted within 3 days of treatment; hence, this dynamically maintained structure can be disassembled by turning off cell-cell signaling (Fig. 3D).

A single-genotype circuit that induces cell fate bifurcation and spatial ordering into a two-layer structure

We also wanted to explore whether we could program self-organizing structures that could start from a single cell type. Alternative bistable

Fig. 2. Engineering self-organizing multilayered spheroids. (A to C) Two-layer circuit. (A) An A-type sender cell expressing CD19 ligand induces a B-type receiver cell to express E-cadherin and GFP. (B) SynNotch cell-cell signals drive receiver cells to express E-cadherin (Ecad), which leads to their segregation into a central layer. The system starts with two disordered cell genotypes but organizes to form a structure with two distinct spatial compartments. (C) Images of the spheroid at 1 and 24 hours. See fig. S1 for other data. (D to G) Three-layer circuit. (D) An A-type cell can send signals to a B-type cell using CD19 ligand, which induces expression of E-cadherin (high expression) and GFP_{lig} (surface-expressed GFP). The induced B-type cell can then send reciprocal signals to the A-type cell; GFP_{lig} serves as ligand to stimulate anti-GFP synNotch receptor expressed in the A-type cell. This reciprocal interaction is programmed to drive a low level of E-cadherin and mCherry. (E) Cell fate diagram showing how this program drives a two-step differentiation process in which the A→B synNotch signal first drives conversion of B-type cells to C-type cells that self-adhere and sort to the center of the structure. The sorted C-type cells then present the C→A synNotch signal (driven by GFP_{lig}) to convert spatially adjacent A-type cells into the middle-layer D-type cell (mCherry and low-level E-cadherin expression). A-type cells bifurcate into two phenotypes, depending on their spatial proximity to the C-type cells in the core of the structure. Here, the system starts with two disordered cell genotypes but self-organizes into three distinct cell phenotypes organized into three spatially distinct compartments. (F) Images from the development of the three-layer system from 0 to 20 hours. See fig. S2 and movie S1 for other data and time-lapse videos. (G) Formation of the three-layer structure is disrupted if synNotch signaling is inhibited (using DAPT, a γ-secretase inhibitor) or if cadherins are not driven as outputs. See fig. S3 for more information.



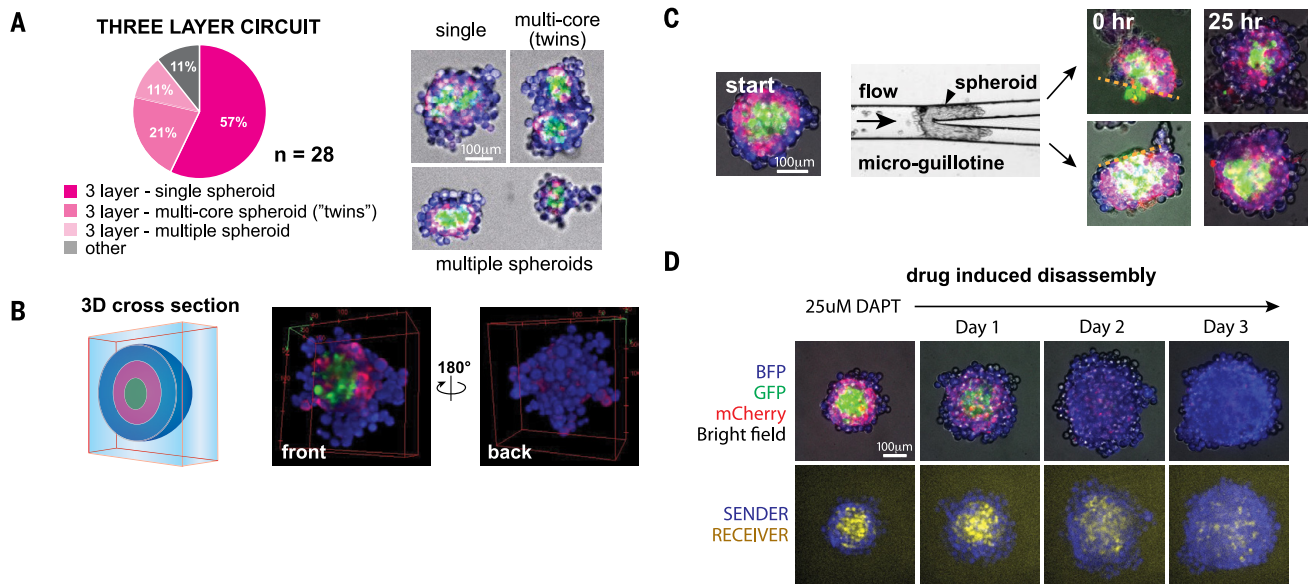


Fig. 3. Three-layer self-organized structure is robust, reversible, and self-repairing. (A) Distribution of structures generated in 28 independent wells (starting with 200 A-type cells and 40 B-type cells). About 90% of the wells showed formation of three-layer structures; the majority of these showed one spheroid per well, with the remainder showing either twinned spheroids or multiple independent three-layer spheroids. Example images of these structural subtypes are shown at the right. (B) Three-dimensional confocal reconstruction of a three-layer structure cross section, shown from two views. See movie S1 for full rotational view of the 3D structure.

(C) Self-repair of a cleaved three-layer structure. The preformed spheroid was cleaved using a microfluidic guillotine, and the two resulting fragments were observed for 25 hours. The frames at 0 hours show the two fragments, with a dotted line indicating the cleavage plane that exposes the internal core of the spheroid. Images at 25 hours show self-repair of the spherical three-layer structure. (D) The structure is reversible if treated with the synNotch inhibitor DAPT. Within 3 days, the differentiation and spatial organization of cells disappeared. Original A- and B-type cells became randomly organized.

Fig. 4. Single-genotype circuit that induces fate bifurcation and spatial ordering into a two-layer structure. (A) Design of single-genotype circuit with lateral inhibition between sender (CD19⁺) and receiver (antiCD19-synNotch-activated) states. The cell encodes both CD19 and anti-CD19 synNotch, but activated synNotch receptor drives expression of tet repressor (tTS), which inhibits CD19 expression. Thus, neighboring cells will drive each other into opposite states indicated by red and green fluorescent markers (fate RED and GREEN).

(B) E-cadherin expression driven from the synNotch-activated promoter. An initially homogeneous population of red cells undergoes bifurcation into RED fate and Ecad-positive GREEN fate by lateral inhibition, and GREEN-fate cells are finally sorted inside to form an inner core. The system starts with a single-genotype population but is expected to organize into a two-layer structure. (C) Purification of a homogeneous population by sorting for mCherry^{high}/GFP^{low} cells. When allowed to communicate through lateral inhibition, the cells rebifurcate into two distinct fluorescently labeled

A **SINGLE GENOTYPE - TWO LAYER CIRCUIT**

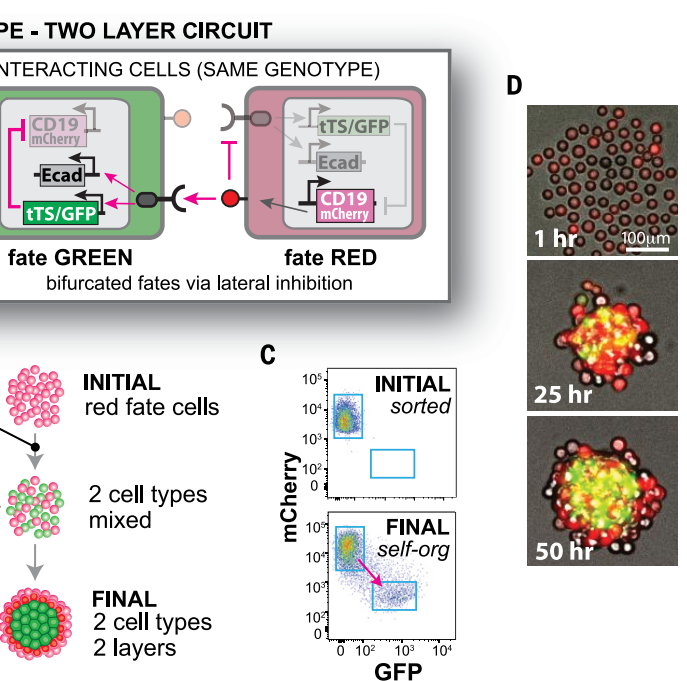
SINGLE GENOTYPE INTERACTING CELLS (SAME GENOTYPE)
αCD19 synNotch
tTS/GFP
Ecad
CD19 mCherry
fate GREEN fate RED
bifurcated fates via lateral inhibition

B

A + A
Ecad + GFP
A^{out} Bⁱⁿ
INITIAL red fate cells
cell type bifurcation
induced Ecad
spatial reorg.
2 cell types mixed
FINAL 2 cell types 2 layers

C

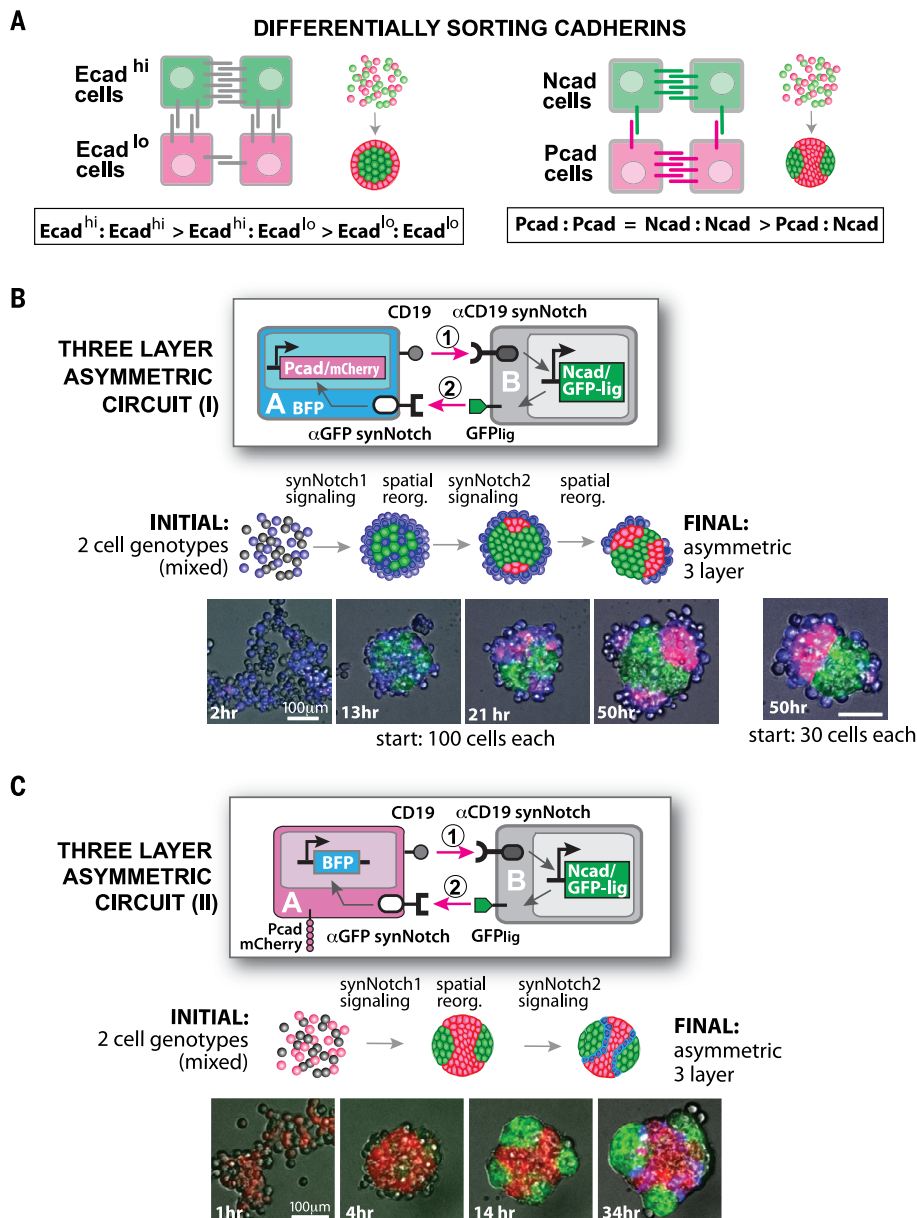
mCherry
INITIAL sorted
FINAL self-org
GFP



populations (bottom). See fig. S4 and supplementary materials for more information on how the lateral inhibition circuit was constructed and executed. (D) Development of the single-genotype two-layer structure. Time frames are shown at 1, 25, and 50 hours, showing initial cell fate bifurcation followed by formation of a stable two-layer structure. See fig. S5 for more information and movie S3 for time-lapse video.

Fig. 5. Programming spherically asymmetric structures by inducing differentially sorting adhesion molecules.

(A) Logic of deploying alternative adhesion outputs to generate different spatial structures. In the spherically symmetric structures of Figs. 2 to 4, we used high and low levels of Ecad expression to define different populations of cells. High- and low-Ecad populations lead to sorting into concentric shells, because Ecad^{lo} cells still prefer to bind Ecad^{hi} cells. In contrast, two cell populations that express either Ncad or Pcad will sort into distinct compartments (nonconcentric) because each of these cadherins prefers homotypic self-association to heterotypic cross-association. **(B)** Three-layer asymmetric circuit I, with the same architecture as that shown in Fig. 2, except that B-type cells are induced to express Ncad and A-type cells are induced to express Pcad. In phase II of the development (reciprocal B→A signaling), the A-type cells become red and self-sort to form one to three external poles (with unactivated A-type cells associated at their periphery). The starting population included 100 cells of each type. When we started with only 30 cells of each type (right image), we reproducibly generated single-pole structures. See fig. S7 and movie S4 for more information, time-lapse videos, and 3D structure. **(C)** Three-layer asymmetric circuit II. An A-type cell constitutively expresses Pcad and mCherry as well as CD19 ligand. B-type cells recognize CD19 with anti-CD19 synNotch receptor, which drives expression of Ncad and GFP_{lig}. In reciprocal signaling, GFP_{lig} drives induction of a BFP marker in A-type cells. Here, the red A-type cells first form a central core and the induced green B-type cells form polar protrusions. A third cell type (blue) forms at the boundary between the red core and the green protrusions. See fig. S8 and movie S5 for more information, time-lapse video, and 3D structure. Information on other structures using different cadherin pairs is shown in figs. S9 and S10 and movies S6 and S7.



cell fates can be generated from a single starting cell genotype through a mechanism known as lateral inhibition (19). For example, cross-repression between Notch receptor and its ligand in neighboring cells can result in a bistable, checkerboard fate pattern, where individual cells bifurcate into either Notch^{active}-ligand^{low} or Notch^{inactive}-ligand^{high} states (20, 21). We built an analogous lateral inhibition circuit using synNotch cross-repression in L929 cells (fig. S4B). Each cell encoded both CD19 (ligand) and the anti-CD19 synNotch receptor, but these are antagonistic to each other because the synNotch receptor induces expression of the Tet repressor (tTS), which can repress CD19 expression (controlled by a TetO promoter). Thus, if synNotch is stimulated by a neighboring cell with high CD19 expression, it will repress CD19 ligand expression, thereby forcing cells to choose between either a sender or receiver fate. CD19 and

tTS expression were monitored by mCherry and GFP, respectively (expressed in linked transcriptional cassettes through a ribosomal skipping porcine teschovirus-1 2A sequence). We established multiple clones that bifurcated spontaneously into two populations of mCherry or GFP-positive cells (fig. S4B; see supplementary materials for details of how we established lateral inhibition lines). These cell lines consistently reestablished the two phenotypic states, even when starting with a pure sorted population of either the red or green state (Fig. 4C and fig. S4B).

To produce a spatially ordered structure from a single cell type, we then functionally combined two different organizational circuit modules: this bifurcating cell fate circuit and the self-organized E-cadherin-driven two-layer circuit (Fig. 2A). To construct such a composite circuit, we expressed E-cadherin from the synNotch-driven promoter

(in addition to inducing expression of the tet repressor) (Fig. 4A and fig. S5A). The objective was to start with a single cell type and observe self-driven fate bifurcation followed by self-driven sorting into two layers.

To track how the system developed from a single cellular phenotype, we sorted red-fate cells (CD19^{high}), placed 100 cells in each well, and followed the development of the spheroid by time-lapse microscopy. These cells developed into a spheroid in which the cells first underwent bifurcation into a red-green checkerboard pattern and then, over the course of hours, formed a two-layer structure with green cells inside and red cells outside (fig. S5, B and C). These two-layer structures were stable for 100 hours. Addition of the Notch signaling inhibitor DAPT prevented fate bifurcation (fig. S5C). But after removal of the drug and re-sorting, the cells remained bipotent; they could still bifurcate and

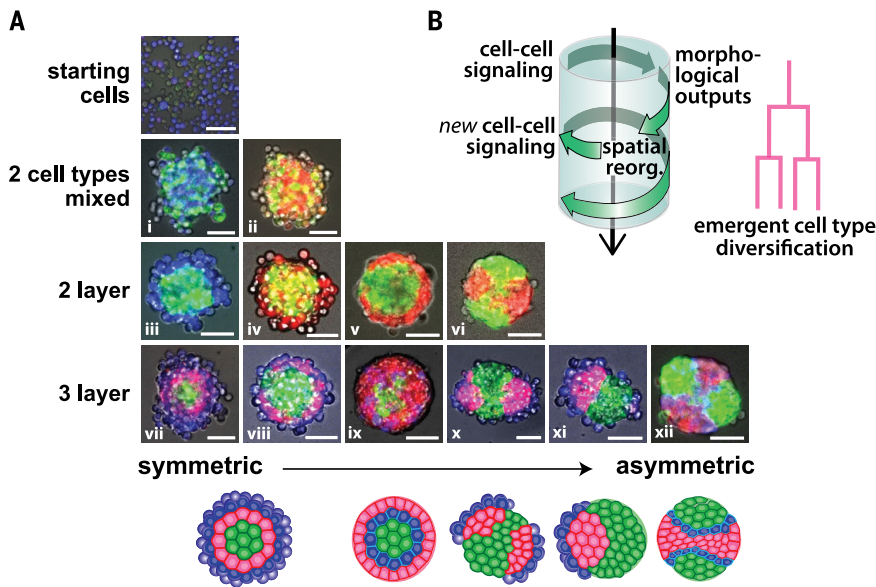


Fig. 6. Gallery of different self-organizing multicellular structures that can be programmed using the simple synNotch→adhesion toolkit.

(A) Gallery of spatially organized behaviors generated in this work, organized by resulting number of cell types and spatially distinct compartments as well as by increasing asymmetry. See table S1 for details of the construction of these 12 structures. Diagrams of several of the different three-layer structures are shown schematically below. (B) These synthetic developmental systems share the common principles in which cascades of cell-cell signaling, linked by morphological responses, lead to increasing diversification of cell types. As signaling drives morphological changes and reorganization, new cell-cell interactions arise, resulting in increasingly distinct positional information encountered by each cell in the structure.

reform the two-layer structure (Fig. 4D, fig. S5C, and movie S3). Thus, we can engineer synthetic programs in which a single cell genotype bifurcates and spatially self-organizes into multiple layers.

Programming spherically asymmetric structures by inducing differentially sorting cell adhesion molecules

Another key feature of natural morphogenesis is symmetry breaking, used repeatedly during development to generate body axes and elaborate an initially uniform ball of cells (22, 23). The structures described above are all spherically symmetric, but we could program asymmetric structure formation with the same signaling cascade circuit by simply changing the adhesion molecules that were expressed.

To build the spherically symmetric three-layer structure described above (Fig. 2D), we programmed different subsets of cells to express different amounts of the same adhesion molecule (E-cadherin), which generates spherically symmetric concentric layers (because $Ecad^{lo}$ cells still prefer to interact with $Ecad^{hi}$ cells; see relative interaction energies in Fig. 5A). However, if cells express different cadherins that have high homotypic affinity but low heterotypic affinity, they phase-separate into two spatially distinct populations (Fig. 5A). N-cadherin (Ncad) and P-cadherin (Pcad) have high homotypic affinity (Ncad-Ncad and Pcad-Pcad) but low heterotypic affinity (Ncad-Pcad) (24), so we used the combination of Ncad and Pcad expression to try to drive asymmetric sorting and structure formation (fig. S6).

We introduced Ncad and Pcad as morphological outputs in the basic three-layer circuit. First, CD19 synNotch signaling from cell A induced expression of Ncad and GFP_{lig} in cell B; second, the induced GFP_{lig} on cell B reciprocally activated anti-GFP synNotch in the adjacent subpopulation of A cells, driving Pcad expression (Fig. 5B, fig. S7, and movie S4). When we cultured 100 cells each of type A and B together, we observed a stereotypical developmental sequence: By 13 hours,

B-type cells expressed both Ncad and GFP_{lig} , and by 21 hours, A-type cells adjacent to B-type cells began to express Pcad and mCherry. Because of the resulting self-segregation of the Ncad- and Pcad-expressing cells, the ensemble self-organized into a nonspherically symmetric three-layer structure (green, red, blue) with one to three distinct poles of mCherry (Pcad) cells. A-type cells (blue) not activated through their anti-GFP synNotch receptors were associated with the outer surface of these poles.

When we initiated cultures with a smaller number of starting cells (30 cells each of type A and B), the ensemble reproducibly formed a single-pole asymmetric structure (a single cluster of red cells instead of multiple clusters), consistent with many examples of polarized organization in which a smaller starting size minimizes the chance of initiation of multiple independent poles (Fig. 5B, fig. S7, and movie S4) (25). Thus, we could reliably program systems that would form three-layer asymmetric or polarized structures.

We designed other circuits that induced alternative types of asymmetric structures with the same Ncad-Pcad output combination but were regulated in different sequential programs. In the circuit shown in Fig. 5C, cell A was similar to the above example (it expressed CD19 ligand and anti-GFP synNotch receptor driving expression of BFP), except that it also constitutively expressed Pcad [connected with mCherry via an internal ribosome entry site (IRES) sequence]. Cell B was the same as in Fig. 5B (it expressed anti-CD19 synNotch receptor that induced Ncad and GFP_{lig} expression). When cultured together, the Pcad-expressing A cells (red) immediately formed an adherent aggregate (4 hours); then, after 14 hours, Ncad and GFP_{lig} were expressed in B-type cells, leading to the formation of polarized B-type protrusions (green) segregated from the A-type cells (red). Finally, at 34 hours, A-type cells at the interface with B-type cells were activated by GFP-synNotch signaling to turn on BFP, resulting in a thin boundary layer of blue cells be-

tween the polarized red and green regions (time-lapse and 3D reconstruction image shown in fig. S8 and movie S5). Additional types of combinatorial circuits using different cadherin pairs are shown in figs. S9 and S10 and in movies S6 and S7.

These results confirmed that we can build various self-organizing structures that break spherical symmetry by inducing distinct self-segregating adhesion molecules in different subpopulations of cells. Initial conditions with small cell numbers can reproducibly yield structures with a single polar axis. Moreover, we can generate many different three-layer morphological structures by altering the combinations of adhesion molecules used and by altering at what stage in the circuit they are expressed (Figs. 5 and 6).

Minimal intercellular communication programs can drive synthetic self-organizing cellular structures

Figure 6A and table S1 summarize the various self-organizing synthetic structures we programmed with our minimal logic of controlling cell adhesion (cadherin expression) through cell-cell communication (synNotch signaling). The diversity and complexity of these structures, and the robustness with which they are formed, illustrate the ordering power of even these highly simplified cell-cell signaling programs. In all of these systems, we observed a cyclic sequence of events in which initial cell signaling interactions induced morphological rearrangements, which in turn generated new cell-cell interactions and new morphological refinements (Fig. 6B). Complex structures emerge because these cell-cell signaling cascades drive increasing cell type diversification.

These diverse emergent structures can form even in the absence of many of the molecular components normally used in natural developmental systems. For example, these circuits do not incorporate diffusible morphogens for cell-cell communication, irreversible cell fate commitment, or direct regulation of cell proliferation, death, or motility (8, 26–29). It is likely that the

synthetic platforms used here could be extended to include many of these additional elements to generate even more sophisticated engineered self-organizing multicellular structures (30–35).

The observation that even minimal circuits that link cell-cell signaling to adhesion can lead to the formation of defined self-organizing structures may help to explain the general principles by which multicellular organisms could have evolved. Choanoflagellates, the closest single-cell relatives of metazoans, have both primitive cadherin and notch genes (36). The cadherin genes are thought to have originally functioned to trap prey bacteria in the environment and may have later been co-opted for cell-cell adhesion (37, 38). In some choanoflagellate species, environmental signals from prey bacteria can induce the formation of multicellular assemblies (39, 40). It seems plausible that cell-to-bacteria adhesion transitioned to cell-cell adhesion, and that bacteria-to-cell signaling transitioned to cell-cell signaling. During the course of evolution, these systems may have begun to regulate one another, providing a starting point for circuits capable of driving formation of complex multicellular structures.

More generally, these findings suggest that it may be possible to program the formation of synthetic tissues, organs, and other non-native types of dynamic, multicellular materials. We may be able to apply tools like synNotch, perhaps enhanced by an even larger toolkit of modular developmental signals, to construct customized self-assembling tissue-like biomaterials of diverse types. These tools and approaches also provide powerful tools to systematically probe and better understand the principles governing self-organization and development.

REFERENCES AND NOTES

1. J. Davies, *Development* **144**, 1146–1158 (2017).

2. M. Elowitz, W. A. Lim, *Nature* **468**, 889–890 (2010).
3. B. P. Teague, P. Guye, R. Weiss, *Cold Spring Harb. Perspect. Biol.* **8**, a023929 (2016).
4. A. Kicheva, N. C. Rivron, *Development* **144**, 733–736 (2017).
5. S. Basu, Y. Gerchman, C. H. Collins, F. H. Arnold, R. Weiss, *Nature* **434**, 1130–1134 (2005).
6. S. S. Jang, K. T. Oishi, R. G. Egbert, E. Klavins, *ACS Synth. Biol.* **1**, 365–374 (2012).
7. M. Rubenstein, A. Cornejo, R. Nagpal, *Science* **345**, 795–799 (2014).
8. L. Wolpert, *J. Theor. Biol.* **25**, 1–47 (1969).
9. D. Gilmour, M. Rembold, M. Leptin, *Nature* **541**, 311–320 (2017).
10. L. Morsut *et al.*, *Cell* **164**, 780–791 (2016).
11. A. Nose, A. Nagafuchi, M. Takeichi, *Cell* **54**, 993–1001 (1988).
12. D. Duguay, R. A. Foty, M. S. Steinberg, *Dev. Biol.* **253**, 309–323 (2003).
13. R. A. Foty, M. S. Steinberg, *Dev. Biol.* **278**, 255–263 (2005).
14. M. Vinci *et al.*, *BMC Biol.* **10**, 29 (2012).
15. C. Chazaud, Y. Yamanaka, *Development* **143**, 1063–1074 (2016).
16. S. E. Harrison, B. Sozen, N. Christodoulou, C. Kyprianou, M. Zernicka-Goetz, *Science* **356**, eaal1810 (2017).
17. A. Sánchez Alvarado, P. A. Tsonis, *Nat. Rev. Genet.* **7**, 873–884 (2006).
18. L. R. Blauch *et al.*, *Proc. Natl. Acad. Sci. U.S.A.* **114**, 7283–7288 (2017).
19. J. R. Collier, N. A. M. Monk, P. K. Maini, J. H. Lewis, *J. Theor. Biol.* **183**, 429–446 (1996).
20. S. J. Bray, *Nat. Rev. Mol. Cell Biol.* **7**, 678–689 (2006).
21. M. Matsuda, M. Koga, K. Woltjen, E. Nishida, M. Ebisuya, *Nat. Commun.* **6**, 6195 (2015).
22. S. Wennekamp, S. Mesecke, F. Nédélec, T. Hiragi, *Nat. Rev. Mol. Cell Biol.* **14**, 452–459 (2013).
23. S. C. van den Brink *et al.*, *Development* **141**, 4231–4242 (2014).
24. J. Vendome *et al.*, *Proc. Natl. Acad. Sci. U.S.A.* **111**, E4175–E4184 (2014).
25. E. Cachat *et al.*, *Sci. Rep.* **6**, 20664 (2016).
26. A. M. Turing, *Philos. Trans. R. Soc. London Ser. B* **237**, 37–72 (1952).
27. M. D. Jacobson, M. Weil, M. C. Raff, *Cell* **88**, 347–354 (1997).
28. E. Scarpa, R. Mayor, *J. Cell Biol.* **212**, 143–155 (2016).
29. E. Li, *Nat. Rev. Genet.* **3**, 662–673 (2002).
30. J. A. Davies, *J. Anat.* **212**, 707–719 (2008).
31. S. A. Newman, R. Bhat, *Int. J. Dev. Biol.* **53**, 693–705 (2009).
32. Y. E. Antebi, N. Nandagopal, M. B. Elowitz, *Curr. Opin. Syst. Biol.* **1**, 16–24 (2017).
33. J. B. A. Green, J. Sharpe, *Development* **142**, 1203–1211 (2015).
34. Y. Hart *et al.*, *Cell* **158**, 1022–1032 (2014).
35. Y. Okabe, R. Medzhitov, *Nat. Immunol.* **17**, 9–17 (2016).
36. N. King *et al.*, *Nature* **451**, 783–788 (2008).

37. M. Abedin, N. King, *Science* **319**, 946–948 (2008).
38. S. A. Nichols, B. W. Roberts, D. J. Richter, S. R. Fairclough, N. King, *Proc. Natl. Acad. Sci. U.S.A.* **109**, 13046–13051 (2012).
39. R. A. Alegado *et al.*, *eLife* **1**, e00013 (2012).
40. A. Woznica *et al.*, *Proc. Natl. Acad. Sci. U.S.A.* **113**, 7894–7899 (2016).

ACKNOWLEDGMENTS

We thank B. Honig and L. Shapiro for discussions regarding cadherin sorting and for providing cadherin plasmids, O. Klein for comments, members of the Lim Lab and the Morsut lab for discussion and assistance, and K. Roybal, M. Thomson, Z. Gartner, W. Marshall, J. Fung, and members of the UCSF Center for Systems and Synthetic Biology and the NSF Center for Cellular Construction. **Funding:** Supported by Japan Society for the Promotion of Science (JSPS) Overseas Research Fellowships (S.T.); a Human Frontiers of Science Program (HFSP) (S.T. and L.M.); a European Molecular Biology Organization (EMBO) Postdoctoral Fellowship (L.M.); NIH grants K99 1K99EB021030 (L.M.), 5P50GM081879 (W.A.L.), and T32GM008412 (L.R.B.); NSF DBI-1548297 Center for Cellular Construction (W.A.L. and S.K.Y.T.); the DARPA Engineered Living Materials program; and the Howard Hughes Medical Institute (W.A.L.). **Author contributions:** S.T. developed and planned research, carried out the design, construction, and testing of self-organizing circuits, and wrote the manuscript; L.R.B. designed and built the microfluidic guillotine and executed experiments for testing regeneration; S.K.Y.T. designed and conceptualized the microfluidic guillotine; L.M. developed and planned research and wrote and edited the manuscript; and W.A.L. developed, planned, and oversaw research and wrote and edited the manuscript. **Competing interests:** The synNotch platform has been patented (U.S. Patent 9,670,281) by the Regents of the University of California and is licensed by Gilead Biosciences. W.A.L. has a financial interest in Gilead Biosciences. **Data and materials availability:** All constructs will be made available on Addgene, and all relevant data are included within the main paper or the supplementary materials.

SUPPLEMENTARY MATERIALS

www.sciencemag.org/content/361/6398/156/suppl/DC1
Materials and Methods
Figs. S1 to S10
Table S1
Movies S1 to S7
References (41, 42)

17 January 2018; accepted 22 May 2018
Published online 31 May 2018
10.1126/science.aat0271



NEW

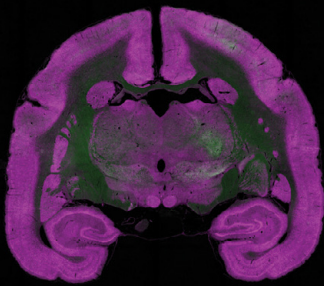
A1 R HD25

Confocal Microscope

See the Bigger Picture

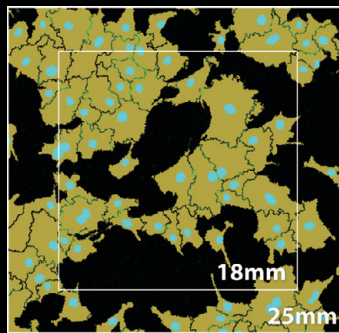
Introducing the A1R HD25, a high-definition, advanced confocal system with twice the field of view of conventional point scanners.

Capturing images of large samples such as tissues, organs and whole organisms requires extending both the detectable area as well as increasing image capture speed. Nikon's new A1R HD25 confocal microscope has the largest field of view (25 mm) on the market, enabling users to explore beyond the traditional boundaries of confocal imaging.



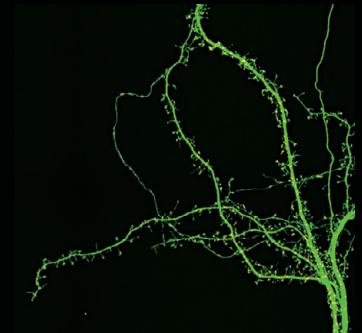
LARGE IMAGES REDEFINED

Faster image stitching with fewer frames.



2X THE DATA IN EVERY SHOT

Acquire twice the data in each frame for faster experiments and better statistics.



STUNNING HIGH DEFINITION IMAGES AT RESONANT SPEED

High-resolution imaging up to 1K x 1K.



25MM FOV

Largest FOV of any commercial point-scanning confocal microscope.



HD RESONANT SCANNER

With redesigned electronics, the HD scanner produces beautiful images at incredible speeds.



MORE DATA, FASTER

Enlarged FOV + high quality resonant scans = more data in less time



ENHANCED DECONVOLUTION

Exclusive deconvolution algorithms based on real data from Nikon optics.



OPTICAL SUPERIORITY

The A1R HD25 was produced through a full redesign with optical performance as the focus.



NIS-ELEMENTS SOFTWARE

Powerful tools for acquisition, analysis and data sharing.

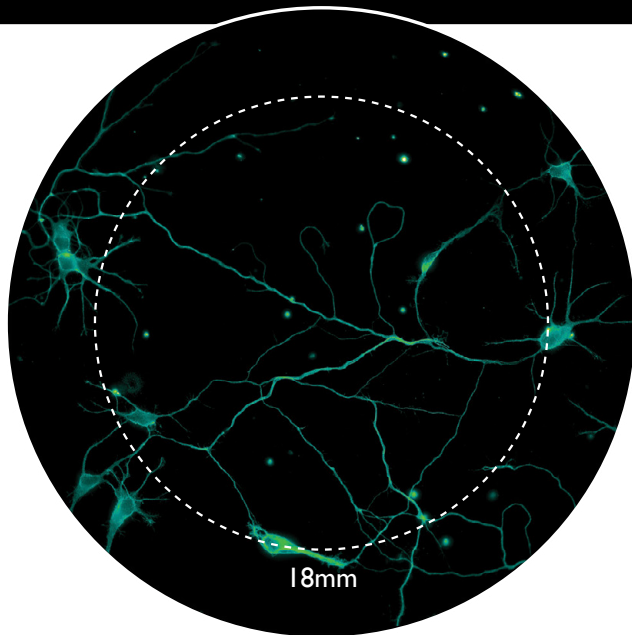
For more information, go to www.microscope.healthcare.nikon.com/a1hd25 or call 1-800-52-NIKON





See More Than Before

Capture 2x More Data in a Single FOV



25mm

18mm

Nikon has raised the bar for core imaging capability with the Eclipse Ti2 Inverted Research Microscope. With its unprecedented 25mm field of view, the Ti2 captures twice as much data with a single image.

There's so much more! For more information, go to www.microscope.healthcare.nikon.com/ti2 or call 1-800-52-NIKON

ECLIPSE
Ti2
Inverted Microscope

